Interim Contractor Report #24

02/01/00 - 02/29/00

Investigation of the Large Scale Evolution and Topology of Coronal Mass Ejections in the Solar Wind

Dr. Pete Riley
SAIC
10260 Campus Point Dr.
MS E3X
San Diego, CA 92121

SciberNet, Inc.
5414 Oberlin Drive, Suite 251
San Diego, CA 92121

Final Report for subcontract Sci–0201–99 (NASW–98007)
for the period: 03/01/99 – 02/29/00

Investigation of the Large Scale Evolution and Topology of Coronal Mass Ejections in the Solar Wind

Pete Riley
SAIC
10260 Campus Point Dr.
MS M3W
San Diego, CA 92121

Abstract

This investigation (subcontract Sci–0201–99 of contract NASW–98007) is concerned with the large–scale evolution and topology of coronal mass ejections (CMEs) in the solar wind. During this reporting period (03/01/99 – 02/29/00) we have focused on several aspects of CME properties, their identification and their evolution in the solar wind. The work included both analysis of Ulysses and ACE observations as well as fluid and magnetohydrodynamic simulations. In addition, we analyzed a series of "density holes" observed in the solar wind, that bear many similarities with CMEs. Finally, this work was communicated to the scientific community at three meetings and has led to three scientific papers that are in various stages of review.

Summary of Work

In this section we summarize the main topics of research undertaken during the past year. This work included: a re–analysis of CMEs observed by Ulysses; an analysis of "density holes" by WIND and ACE; an investigation of the relationship between electron density and temperature within CMEs; and fluid simulations of CME–driven disturbances.

In addition to these main areas of work, our work also included:

(1)A collaboration with Geraint Jones at Imperial College to identify the cause and origin of Planar magnetic structures in the Ulysses data set. Our working interpretation is that they represent the "legs" of CMEs.
(2)Mapping in situ solar wind data back to the Sun using fluid and MHD simulations to localize the origin of CMEs and other transient phenomena.
(3)Regular viewing of Ulysses data set for CME–related events.
(4)Development of an algorithm to automatically detect CME–related events in situ plasma and magnetic field data sets. So far, we have focused on identifying fast forward shocks preceding CMEs.

<u>Re–analysis of CMEs observed by Ulysses during it's en–ecliptic phase of the mission</u>

There is a long standing debate on the most appropriate techniques for analyzing interplanetary shocks, and in particular, concerning the calculation of the orientation of shock fronts. Two approaches are most often used; magnetic coplanarity and velocity coplanarity. Magnetic coplanarity utilizes the upstream and downstream magnetic fields to calculate the local orientation of the shock. The approach is exact (at least within the approximations of MHD) and the magnetic field is typically measured at much higher resolution than plasma parameters. However, fluctuations in the magnetic field components typically make its determination difficult. Velocity coplanarity, on the other hand, is only an approximate result, most valid for nearly perpendicular shocks and relies on velocity measurements, which are typically separated by several minutes.

Based on referee's comments to a paper we submitted during year 1 of this contract, we re–analyzed the shocks observed by Ulysses during its in–ecliptic passage to Jupiter using magnetic coplanarity and compared the results with the previously applied velocity coplanarity approach. Significant quantitative differences were found between the two methods. Nevertheless, the conclusions reached in the paper were unchanged; that is, there is a preponderance of westward and northward tilts to the shock normals and the shock speed decreases with increasing heliocentric distance.

It is still not clear which approach is most appropriate for interplanetary shocks. If the goal is to determine other shock parameters (speed, strength, etc.), in addition to the orientation of the front, then the disparity in resolution is of secondary importance, since the plasma data must be utilized. We have previously shown that errors in neglecting the magnetic field can translate into as much as ~20% errors in the determination of the shock orientation. However, the contribution of waves and turbulence to the magnetic

field and their effect on the coplanarity of the field cannot be easily determined. The consensus within the space physics community is that magnetic coplanarity is the better approach, and so we chose to include this method in our revised paper. This comparison, however, suggests that a detailed quantitative study of these two methods, including the analysis of realistic synthetic shocks, is necessary. The results of this analysis were included into a revised version of the manuscript. It was accepted for publication in the *Journal of Geophysical Research* in January, 2000 and is included in appendix 1.

Fluid aspects of solar wind disturbances

Near the Sun, Coronal Mass Ejections (CMEs) exhibit a wide range in propagation speeds, ranging from ~50 km/s to > 2000 km/s. Moreover, half of the CMEs observed within 5 solar radii by the coronagraph onboard the Solar Maximum Mission over a 7 year period, had speeds less than 300 km/s; a result independent of heliographic latitude. By comparison, the average speed of the low latitude solar wind at 1 AU is ~440 km/s. Thus even within the slow solar wind, it is likely that a significant fraction of CMEs are traveling at speeds, at least initially, lower than the ambient solar wind. We have previously investigated the acceleration of slow CMEs embedded within a fast solar wind, indicative of the high–latitude solar wind flow using 1–D gas–dynamic simulations and comparing with Ulysses observations of high latitude CMEs. We found that pressure gradients induced by the initial speed differences between the slow CMEs and the faster ambient solar wind flow generated large accelerations of the CMEs, eventually bringing them up to the speed of the ambient solar wind flow over scales of 1 to 10 AU.

In the present study, we investigated the acceleration of even slower CMEs embedded within a slow flow indicative of the low–latitude, slow solar wind. We generated an ambient solar wind flow of approximately 440 km/s, and launched a velocity pulse into the inner boundary (at 30 solar radii) consisting of a drop in speed of 250 km/s over an interval of 15 – 20 hours. We considered both square and bell–shaped pulses (which alter the evolution of the disturbances quantitatively. However, they were used primarily as a check that the qualitative results are not dependent on the shape of the pulse). Our results demonstrated that the CMEs are accelerated up to ambient solar winds considerably faster than their high–latitude counterparts. In fact, for the range of inputs considered, the CMEs reach ambient solar wind speeds within a fraction of an AU. The rapid formation and propagation of a compression region at the trailing edge of the CME produces this acceleration. These results, together with others are summarized in a paper submitted to the *Journal of Geophysical Research*, and included in appendix 2.

Relationship between electron density and temperature within CMEs

Osherovich and colleagues have argued that the relationship between electron number density and temperature within magnetic clouds (and CMEs in general) suggests that the adiabatic index is less than one. Others, such as J. T. Gosling, have argued that such a conclusion is not reasonable, since it requires that the temperature within CMEs increases with increasing distance from the Sun. At the heart of the debate, is the question of whether one can infer an adiabatic index from a single slice through a CME. For, under

such circumstances, one is not monitoring the variation in a parcel of plasma, but snapshots of different plasma.

We investigated the relationship between temperature and density using a series of 1–D, where we simulated CME–like pulses and tracked their evolution through the solar wind. The simulation region ranged between our inner boundary, at 30 solar radii, and our outer boundary, at 5 AU. We specified inflow boundary conditions at the inner edge and allowed the system to relax into an equilibrium solution. Into this solution, we propagated a pulse mimicking a CME. We varied the duration, speed, density, and/or temperature variations of the pulse. It is important to realize that the equations strictly assume a polytropic relationship between density and temperature. Thus if we set the adiabatic index, gamma = 1.5 in the simulation, then this value holds for all elements of plasma at all times and at every point within the simulation. We launched several test pulses into this ambient solution and found that plots of Log(density) versus Log(temperature) at particular distances can, although not always, display slopes different from 0.5 (the slope of the points gives (gamma–1), thus gamma = 1.5 would produce a slope of 0.5) within the pulse. Thus our interpretation is that the slope is not necessarily indicative of the value of the adiabatic index. The details of these simulations are covered in more detail in a paper to be submitted to the *Journal of Geophysical Research*, and included in appendix 3.

Analysis of "density holes"

We analyzed a series of low density intervals in the ACE and WIND plasma data. At least one of these events (May, 1999) has been associated with significant geomagnetic activity at Earth and was the topic of several sessions at the Fall AGU meeting in San Francisco, as well as several popular media reports (also known as "the day the solar wind disappeared"). Although the cause of these events remains unclear, we believe they may represent some type of transient activity akin to coronal mass ejections. Using a 3–D MHD model, we modeled the structure of the solar corona during the intervals containing these density holes. Although the model is not yet capable of initiating the types of perturbations that we believe are responsible for these density holes, it can in principle provide a picture of the underlying equilibrium structure of the corona during these times. We mapped the density holes from their interplanetary location back to the solar corona and found that all events were associated with low density regions in the corona. Moreover, a current sheet crossing could be identified immediately preceding a low density region as was observed in some of the events. Thus we believe that the models provide a reasonable approximation to the equilibrium structure of the solar wind. We suggest that this configuration must be present in order for a low density transient to be initiated. This could explain why we also see low density regions in the model that do not apparently map out to low density events in the solar wind: In addition to this equilibrium configuration, a transient process is also required to initiate the event, in much the same way as a CME is launched. The results of this work were presented at the Fall American Geophysical Union meeting in San Francisco, December, 1999 by Dr. Barbara Thompson in a talk entitled "The Structure of the Sun During Low–Density Solar Wind Periods". We plan to write up this research during the next several months and submit to a special issue of *Geophysical Research Letters*.

Scientific Presentations and Papers

During the past year, the results of this investigation were presented at three scientific meetings:

(1) An oral summary of the work outlined here was made at the Ulysses Science Working Team meeting in San Diego in October, 1999 .

(2) An oral presentation on the simulations performed to investigate the origin of density holes in the solar wind was presented by Dr. B. Thompson at the Fall AGU meeting, San Francisco, in December, 1999.

(3) An oral presentation on Ulysses and WIND plasma observations, including the identification of CMEs, was presented at the Whole Sun Month III workshop at the Goddard Spaceflight Center, Maryland, in January, 2000. "

Three papers were completed, submitted, or accepted based on the work performed in this investigation:

(1) Properties and radial trends of coronal mass ejecta and their associated shocks observed by Ulysses in the ecliptic plane by Pete Riley, J. T. Gosling, D. J. McComas, and R. J. Forsyth.

(2) Fluid aspects of solar wind disturbances driven by coronal mass ejections by J. T. Gosling and Pete Riley

(3) On the polytropic relationship between density and temperature within CMEs: Numerical simulations by Pete Riley, J. T. Gosling, and V. J. Pizzo

These papers are included in the appendices.

APPENDICES

Appendix 1

Properties and radial trends of coronal mass ejecta and their associated shocks observed by Ulysses in the ecliptic plane

Pete Riley, J. T. Gosling, D. J. McComas, and R. J. Forsyth

Accepted for Publication in the *Journal of Geophysical Research*, January, 2000

Properties and radial trends of coronal mass ejecta and their associated shocks observed by Ulysses in the ecliptic plane

Pete Riley
Science Applications International Corporation, San Diego, California

J. T. Gosling and D. J. McComas
Los Alamos National Laboratory, Los Alamos, New Mexico

R. J. Forsyth
The Blackett Laboratory, Imperial College, London, United Kingdom

Short title: CMES AND THEIR ASSOCIATED SHOCKS

Abstract. In this report, magnetic and plasma measurements are used to analyze 17 interplanetary coronal mass ejections (CMEs) identified by Ulysses during its in-ecliptic passage to Jupiter. We focus on the expansion characteristics of these CMEs (as inferred from the time rate of change of the velocity profiles through the CMEs) and the properties of 14 forward shocks unambiguously associated with these CMEs. We highlight radial trends from 1 to 5.4 AU. Our results indicate that the CMEs are generally expanding at all heliocentric distances. With regard to the shocks preceding these ejecta, we note the following: (1) there is a clear tendency for the shock speed (in the upstream frame of reference) to decrease with increasing heliocentric distance as the CMEs transfer momentum to the ambient solar wind and slow down; (2) 86% of the shock fronts are oriented in the ecliptic plane such that their normals point westward (i.e., in the direction of planetary motion about the Sun); (3) 86% of the shocks are propagating toward the heliographic equator; and (4) no clear trend was found in the strength of the shocks versus heliocentric distance. These results are interpreted using simple dynamical arguments and are supported by fluid and MHD simulations.

1. Introduction

The Ulysses spacecraft was launched in October 1990 and during the next sixteen months traveled outward to Jupiter where it received a gravitational assist necessary to propel it into a polar orbit about the Sun. During this near-ecliptic phase of the mission, at least 25 coronal mass ejections (CMEs) were encountered [*Phillips et al.*, 1997].

In this report, we analyze the expansion characteristics of these ejecta and the properties of the shocks associated with them and attempt to identify radial trends. Specifically, we focus on the speed profiles within the ejecta which allow us to determine the expansion properties of the ejecta, and we compute the orientation, speed, and strength of the 14 fast-mode forward shocks that could be unambiguously associated with these ejecta.

Several previous studies have analysed specific CME-driven events during the in-ecliptic phase of the Ulysses mission (e.g., *Phillips et al.* [1992]; *Lanzerotti et al.* [1992]). Other studies have summarized the properties of shocks observed during this period, but did not distinguish between corotating and CME-associated shocks [e.g., *Burton et al.*, 1992; *Balogh et al.*, 1995]. Several studies have summarized the general properties of these transient events. *Phillips et al.* [1997] provided a list of the CMEs, including start times, and possible associations with transient shocks. *González-Esparza et al.* [1998] analyzed several dynamic properties of these CMEs and, in particular, found an apparent lack of correlation between the radial widths of the ejecta and heliocentric distance. The authors interpreted this result as an indication that the ejecta had established a pressure equilibrium with the surrounding ambient solar wind and were no longer expanding. In contrast, *González-Esparza and Bravo* [1998] compared Ulysses observations with near-Earth IMP observations to infer that the radial width of the ejecta was larger at Ulysses than at IMP, demonstrating that the ejecta were expanding as they propagated away from the Sun.

In an earlier study, *Gosling et al.* [1987] examined the flow properties at the leading edge of 19 fast CMEs using data from ISEE 3. They found that 17 events displayed eastward flow deflections across the leading edge of the ejecta. Thus the normal vectors to the ejecta fronts were tilted toward the west (i.e., in the direction of planetary motion). In contrast, no pattern was found in the meridional flow deflections. The authors proposed that the observed eastward flow deflections were a consequence of solar rotation and the Parker spiral pattern that resulted from it. As the ejecta propagate approximately radially outward from the Sun, westward pressure gradients acted to 'refract' the ejecta fronts so that they became more aligned with the prevailing Parker spiral.

The data analyzed in this study derives from the Solar Wind Over the Poles of the Sun (SWOOPS) ion sensor [*Bame et al.*, 1992] and the magnetometer instrument [*Balogh et al.*, 1992] onboard the Ulysses spacecraft. The plasma moments produced from the SWOOPS instrument have a typical resolution of 4–8 minutes, while the magnetic field field components have a typical resolution of 1–2 seconds.

This report is structured as follows. In section 2 we discuss the expansion characteristics of the ejecta. In section 3 we describe the analysis techniques that were performed on the transient forward shocks and discuss the results of this analysis. Finally, in section 4 we discuss the results of this study and compare with numerical models of CME evolution.

2. Plasma Characteristics of the Ejecta

The coronal mass ejections encountered by Ulysses during its outward passage to Jupiter were identified primarily by the presence of counterstreaming suprathermal electrons (CSEs) [*Phillips et al.*, 1997]. In addition, these authors required that at least one other characteristic commonly associated with ejecta (e.g., anomalously low proton temperature [e.g., *Gosling et al.*, 1973] or high helium abundance [e.g., *Hirshberg et al.*,

1972]) also be present. These combined criteria led to the identification of 25 CMEs. However, among these events there was considerable variability. Many, for example, did not display helium abundance enhancements or rotations in the magnetic field, which are commonly associated with flux ropes. In some cases, the boundaries of the ejecta were difficult to ascertain.

To mimimize variability due to different trajectories through the CME-driven disturbances, we restrict our analysis to only those events for which at least two other plasma and/or magnetic field signatures were present in addition to the signature of CSEs. By so doing, our initial list of 25 events was reduced to 17. Table 1 summarizes all 25 CMEs that were observed by Ulysses during its transit to Jupiter. Columns 1 and 2 provide the inferred start dates and times and columns 3 and 4 provide the inferred stop dates and times. Column 5 indicates whether a fast forward shock was obviously associated with the ejecta and column 6 indicates whether the CME was included in the current study.

Figure 1 shows the speed profiles for the 17 CMEs. In each case, speed is plotted as a function of time in days, as indicated by the legend in the upper left. The first two CMEs occurred in 1990, the last two occurred in 1992, and the remaining events occurred in 1991. In each panel, the data begin at the leading edge of the ejecta (left) and end at the trailing edge (right). Superimposed on each plot is a least squares fit to the data. A negative slope indicates that the leading edge of the CME is travelling faster than the trailing edge. Furthermore, if the change between the two boundaries is relatively monotonic, then the CME is expanding; 71% (12 of 17) of the events displayed negative gradients, indicating that the majority of the ejecta were expanding. Presumably the positive gradients in the remaining events are the result of compression and acceleration of the ejecta by faster solar wind behind the CME.

Using the least squares fits calculated above, we can define an 'expansion rate' for each CME as $-dv/dt$. We emphasize, however, that since we measure the CME

parameters at a single point in space, this 'rate' is in reality a convolution of both temporal and radial effects. Furthermore, $-dv/dt$ is likely to be sensitive to a number of intrinsic properties of the CMEs, as well as properties of the ambient solar wind into which the CMEs are propagating. Simulation results (e.g., *Gosling et al.* [1995b]; *Riley et al.* [1997]; *Riley and Gosling* [1998]) illustrate that the relative speed between the ejecta and the ambient solar wind can have a substantial impact on the rate of expansion of CMEs. Thus, in an effort to minimize scatter and amplify any underlying trends, we further restrict our analysis to those ejecta that were propagating sufficiently fast to drive a forward shock. Figure 2a shows $-dv/dt$ for the 14 events that were unambiguously associated with shocks (see Table 1). Eleven of the 14 events lie above zero indicating expansion. The least-squares fit to the points suggests that the rate at which CMEs expand tends to decrease with increasing heliocentric distance. However, this fit may be biased by several events observed at ~ 2.3 AU (corresponding to the time period March–April, 1991, during which time there was major solar activity [*Phillips et al.*, 1992]). Thus at best, these results should be viewed tentatively.

It is straightforward to show that for fast plasma outrunning slower plasma ballistically (i.e., such that each parcel of plasma maintains constant speed), a gradient evolves between them such that $dv/dt \propto 1/R$, where R is the heliocentric distance of the ejecta. In reality, however, dv/dt will decrease faster than $1/R$ as a rarefaction (or expansion wave) propagates into the surrounding plasma. On the other hand, if the expansion of the ejecta is impeded by the surrounding plasma, dv/dt would decrease less rapidly than $1/R$. Thus in Figure 2b we display $-Rdv/dt$ as a function of heliocentric distance. The large scatter and lack of any obvious trend does not allow us to infer an expansion rate appreciably different from $1/R$.

3. Shock Analysis

We now turn our attention to an analysis of the transient forward shocks associated with these ejecta. In particular, there are several methods for calculating the orientation of shock fronts [*Abraham-Shrauner and Yun*, 1976]. The two approaches most often used are magnetic coplanarity and velocity colinearity. Velocity colinearity is only an approximate result that is most valid when the shock is nearly perpendicular and the magnetosonic Mach number is high [*Abraham-Shrauner and Yun*, 1976]. The errors associated with this method have been discussed in detail by *Riley et al.* [1996]. Magnetic coplanarity is, on the other hand, at least theoretically an exact method. However, while this is true for nearly perpendicular shocks, the technique can become inaccurate as the angle between the upstream and downstream magnetic field vectors, $\mathbf{B}_1$ and $\mathbf{B}_2$, becomes small. This is especially true when large fluctuations exist, as are often observed in solar wind magnetic field measurements. In this study, we use magnetic coplanarity to determine the orientation of the shock normal, $\mathbf{n}$:

$$\mathbf{n} = \pm \frac{(\mathbf{B}_1 \times \mathbf{B}_2) \times (\mathbf{B}_1 - \mathbf{B}_2)}{|(\mathbf{B}_1 \times \mathbf{B}_2) \times (\mathbf{B}_1 - \mathbf{B}_2)|} \tag{1}$$

Typically, in the analysis of interplanetary shocks, windows upstream and downstream of the shock are chosen and the plasma and magnetic field parameters are first averaged before calculating the properties of the shocks. However, because of potential contamination by waves, the approach we adopt is to match all the points in the upstream region with all the points in the downstream region and calculate $\mathbf{n}$ for each. Thus for p points upstream and downstream we actually calculate p^2 unit normals. Since $\mathbf{n}$ is a unit vector, it can be expressed as a function of two coordinates (θ, ϕ). θ is defined as the latitudinal angle and is positive northward. ϕ is defined as the azimuthal angle and is positive in the direction of planetary motion about the Sun. Thus, the radial direction is represented by (0,0). Since the distributions of calculated

unit normals tend to be fairly circular in (θ, ϕ) space for any given shock, we assume that $\mathbf{n} = (< \theta >, < \varphi >)$. Each shock calculation is checked by visually inspecting the cluster of normals in the (θ, ϕ) plane. This technique has been used previously to calculate the orientation of interplanetary corotating shocks [*Riley et al.*, 1996; *Gosling et al.*, 1997] as well as the orientation of the polar coronal hole boundary [*McComas et al.* 1998] using velocity colinearity.

Once the orientation of the shock front has been determined, we use mass conservation to determine the speed of the shock in the spacecraft frame of reference:

$$v_{shock} = \frac{1}{p} \sum_{i=1}^{p} \frac{\Delta [N_i \mathbf{v}_i] \cdot \mathbf{n}}{\Delta [N_i]} \tag{2}$$

where N_i is the proton number density, and $\mathbf{v}_i$ is the proton velocity in the spacecraft frame of reference. $\Delta [...]$ denotes the difference between the downstream and upstream quantities and the summation over i runs over p measurements. It is usually more meaningful to discuss the speed of the shock relative to the upstream solar wind (v^*_{shock}) which is obtained by subtracting $v_1 \cdot \mathbf{n}$ from the right hand side of (2).

Following *Gosling et al.* [1995a], we define the shock strength, χ_{ss}, to be the ratio of the downstream to upstream density minus 1:

$$\chi_{ss} = \frac{N_2}{N_1} - 1 \tag{3}$$

This definition of χ_{ss} is such that for an infinitely weak shock, $\chi_{ss} \rightarrow 0$. From simple theoretical considerations we would predict a maximum value, $\chi_{ss} \sim 3$ when the ratio of specific heats, $\gamma = \frac{5}{3}$.

The difference between the resolution of the magnetic field measurements (1–2 s) and the plasma measurements (4–8 min) makes the choice of upstream and downstream windows difficult. On one hand, the windows should be sufficiently narrow and close to the shock front so as to reduce potential contamination by waves and/or discontinuities.

On the other hand, the windows must be sufficiently wide and/or far away from the shock front so as to include at least one meaningful plasma data point. Our approach was to analyze each event by hand, choosing the windows so as to: (1) minimize the scatter in plots of $\mathbf{n}$ in (θ, ϕ) space; and (2) include at least one representative plasma data point within each window. As a check, we also applied velocity colinearity to larger windows to determine the shock normal, shock speed, and shock strength. Although we found quantitative differences between the two approaches, the conclusions reached in the study were insensitive to the particular technique. A detailed comparison of these, as well as other techniques will be presented elsewhere.

The 14 shocks used in this study are listed in Table 2. All were (fast-mode) forward shocks that preceded CMEs by anywhere from 4 hours to 2.5 days. All events fit the paradigm of a fast ejecta plowing through a slower ambient solar wind and driving a shock wave ahead.

Figure 3 presents shock speed, in the upstream solar wind reference frame, as a function of heliocentric distance. The numerical values are summarized in Table 2. Although there is significant scatter, the trend is for shock speed to decrease with increasing distance from the Sun. The dashed line represents a least squares fit to the points.

Figure 4a presents the shock strengths, as defined by equation (3). There appears to be no obvious trend with increasing distance from the Sun. Shock strength is, however, one of the least accurately determined shock parameters, and is likely to be more sensitive to the initial properties of the individual ejecta (i.e., mass and speed). For comparison, Figures 4b and 4c display the ratio of downstream to upstream magnetic field strength and the magnetosonic Mach number as calcuated by *Balogh et al.*, [1995]. These parameters provide an independent verification of a lack of trend in shock strength with heliocentric distance. It is also noteworthy, and reassuring, that there is a relatively good correlation between point-to-point variations in the parameters, in spite

of the fact that the windows were chosen independently.

In Figure 5, we have computed the sound speed (c_s), Alfvén speed (v_A), and magnetosonic speed (v_s) immediately upstream of each shock. Of interest here is the modest (17 km s^{-1}) decrease in the magnetosonic wave speed, which is driven primarily by a decrease in the Alfvén speed.

Figure 6 displays the orientations of the shock normals. The top panel presents shock tilts in the meridional plane. Twelve of the 14 events have a positive tilt. Thus 86% of the shock normals are tilted northward in the meridional plane. Since Ulysses' trajectory was displaced southward of the heliographic equator during this period, we infer that the shock normals were also tilted preferentially toward the heliographic equator. The bottom panel shows shock orientations in the azimuthal plane. From this, we deduce that 86% are also tilted toward the west (although the two events that are tilted toward the east are not the same two events that are tilted toward the south).

4. Summary and Discussion

In this study, we have analyzed the expansion properties of 17 coronal mass ejections observed by Ulysses during its outward bound trip to Jupiter and computed the basic shock parameters of 14 transient forward shocks that were associated with these ejecta.

Our results indicate that CMEs are generally expanding as they propagate away from the Sun and that the rate of expansion tends to decrease with increasing distance from the Sun. This is not a surprising result; coronagraph observations indicate that CMEs near the Sun are expanding. They are inferred to have pressures considerably higher than the ambient solar wind into which they are propagating. Thus initially, the high pressure within the ejecta drives a strong expansion, but as the CME propagates farther from the Sun and evolves toward pressure balance with the ambient solar wind, the rate of expansion decreases. CME expansion in the solar wind may also be the

result of other effects [e.g., *Gosling and Riley*, 1996]. For example, CMEs travelling faster than the trailing ambient solar wind, and/or slower than the leading wind expand as they are accelerated into the rarefaction caused by the difference in speed between the CME and the ambient solar wind. Also, expansion may simply be the result of the leading edge of the CME being ejected faster than the trailing edge. Unfortunately, the scatter in the calculated expansion rates precludes us from inferring an expansion rate significantly different from $1/R$, which would be expected based on the evolution of ballistic trajectories.

Our results may be compared with a study by *González-Esparza et al.* [1998] who examined the variation in the radial width of these ejecta (computed by integrating the solar wind bulk speed between the leading and trailing edges of the ejecta) as a function of heliocentric distance and concluded that there was no evidence for expansion between 1 and 5 AU. Their method, however, was sensitive to a number of factors, including the initial intrinsic properties of the CMEs and the trajectory taken by the spacecraft through the event. On the other hand, our approach provides a more direct measure of expansion since clearly a CME is expanding if its leading edge is moving faster than its trailing edge. Our results support the study by *González-Esparza and Bravo* [1998] who found that ejecta observed by both Ulysses and IMP displayed larger radial widths at larger heliocentric distances.

As a fast CME plows through the solar wind travelling at speeds (in the rest frame of the upstream solar wind plasma) in excess of the fast magnetosonic wave, it drives a shock ahead of it, providing the necessary mechanism to communicate the presence of the outward-moving CME to the solar wind ahead. Momentum coupling, however, between the ejecta and the slower leading and trailing solar wind acts to slow the ejecta down. In turn, the speed of the shock relative to the upstream solar wind diminishes. Our results suggest that, on average, the rate of change in velocity with distance is ~ 15 km s^{-1} AU^{-1}. However, for any particular event, the rate of deceleration is likely to be

sensitive to the initial properties of the ejecta as well as the ambient wind into which it is propagating.

Our results suggest that there is no underlying trend in the strength of shocks (as defined by the ratio of downstream density to upstream density) preceding a fast CME as a function of heliocentric distance. This is supported by a comparison of the variation of B_d/B_u and the magnetosonic Mach number with heliocentric distance as calculated by *Balogh et al.* [1995]. We suggest that the competing effects of: (1) the shock slowing down; and (2) the characteristic wave speed of the upstream solar wind decreasing conspire to produce this result. Both of these effects are evident in the data, although the decrease in the magnetosonic wave speed upstream of the shocks is relatively modest.

To explore whether one might expect to observe a systematic variation in shock strength with distance from the Sun we have utilized one-dimensional (1-D) fluid simulations of fast transient disturbances. In simulating CIR evolution, 2- and 3-D effects have been shown to be important in the evolution of shocks bounding interaction regions [*Pizzo,* 1981]. However, fast CMEs propagate radially away from the Sun, suggesting that multi-dimensional effects may not be as significant. This is supported by 2-D [*Riley et al.,* 1997] and 3-D [*Odstcril and Pizzo,* 1999] simulations that show that while the large-scale morphology of ejecta and their associated disturbances are affected by the dimensionality of the simulation, the essential features of the disturbance along some radial trajectory are captured by 1-D results [e.g., *Gosling et al.,* 1995]. The algorithm employed is based on an Eulerian finite difference scheme with inflow boundary conditions specified at the inner boundary ($30R_{Sun}$) and outflow boundary conditions specified at the outer boundary (6 AU) [e.g., *Riley and Gosling,* 1998; *Riley et al.,* 1997]. The simulation region is filled with typical solar wind values and the system is allowed to evolve into an equilibrium. A bell-shaped pulse is then launched at the inner boundary in the form of a speed perturbation while holding the density and

temperature constant.

In Figure 7 we compare two profiles of a pulse mimicking a fast CME-driven disturbance at 83 (1.75 AU) hours and 250 hours (5 AU) following its launch. Over an interval of 10 hours, the speed was raised smoothly by 300 km s^{-1} and then lowered smoothly while holding the remaining plasma parameters constant. The top panel shows speed, the middle panel shows number density, and the bottom panel shows the thermal pressure of the fluid as functions of heliocentric distance. The point to note from Figure 6 is that the strength of the shock at the leading edge of the disturbance (which, by virtue of the logarithmic scaling, is directly proportional to the change in density) does not change appreciably between $\sim 1.75AU$ and $\sim 5AU$. In contrast, the speed of the shock decreased substantially over that distance range. Numerical experiments such as this one were repeated for a variety of speed profiles. For several cases, the simulation region was extended to 50 AU to investigate whether trends might only become apparent over sufficiently large distances. In some cases, the shock strength increased slightly, while in other cases it decreased. However these variations were never more than 10–15%. Thus although shocks slow down as the CME-driven disturbances propagate away from the Sun, the characteristic wave speed of the medium into which they are propagating also decreases and the net effect is that the strength of the shock does not change appreciably over large distances. These results are in qualititative agreement with 1-D simulations of corotating streams by *Hundhausen* [1973] who found that the strength of shocks either remained constant or increased between 1 and 6 AU.

Linearized fluid models [*Burton et al.*, 1992], two-dimensional MHD simulations [*Odstrčil et al.*, 1996], and three-dimensional hydrodynamic simulations [*Odstrčil and Pizzo*, 1999a,b] suggest that the large-scale meridional structure of the ejecta and shock fronts near the eclipic is concave outward. Thus the normal vectors to the fronts are tilted toward the heliographic equator in both hemispheres. Ulysses was located in the southern hemisphere ($\lesssim S6°$ heliographic latitude) during this interval and hence the

northward (i.e., equatorward) tilts of the shock normals are consistent with this picture. Slower denser flow equatorward of the observation acts to retard the disturbance more and thus effectively refracts the shock normal toward the equatorial plane. Thus these orientations imply that at least part of the ejecta was embedded within the streamer belt. Another possibility is that the majority of the ejecta were centered south of the spacecraft. However, this would imply a meridional asymmetry in the launch characteristics of CMEs at the Sun for a period of $\sim$ 16 months.

The inferred azimuthal orientation of the shock fronts is consistent with an earlier study by *Gosling et al.* [1987] of flow deflections at the leading edges of fast ejecta. Taken together, these two studies suggest that these tilts may be a large scale phenomenon. *Gosling et al.* proposed that the azimuthal ejecta tilts may be the result of one (or a combination) of two effects, both related to the Parker spiral pattern. First, as the fast CME sweeps up the ambient solar wind magnetic field ahead, the draping of the field lines takes place asymmetrically, with more draping occurring on the westward side. The net result is an east-west magnetic pressure gradient that causes the ejecta to rotate toward the west. Second, inhomogeneities organized about the Parker spiral could cause the observed azimuthal tilts. In particular, as the fast CME approaches and overtakes the slower, denser material of a slow stream, it will encounter the slow stream at its westward edge first and thus be retarded more there. Three-dimensional hydrodynamic simulations of CME evolution in a simple two-stream tilted dipole model [*Odstrčil and Pizzo,* 1999a,b] support the idea that significant azimuthal tilts can be generated by the prevailing Parker corotating flow pattern. However, this model only predicts the observed westward asymmetry for certain launch characteristics. In particular, the CME must be launched at the eastward edge of the slow-flow stream. Under such conditions, as it moves away from the Sun, it interacts with the slow flow wind as described above. In contrast, if the CME is launched from the center of the slow flow wind, the ejecta can display an eastward tilt. When an ejection is launched to

the west of the slow wind, there is no slow ambient flow ahead for it to interact with; no shock forms and the ejection does not display a significant tilt.

Since inhomogeneities occur in the solar wind on all measurable scales, it is not clear that the observed tilts are global effects; if the ejecta respond only to small-scale inhomogeneities, the fronts may be tilted locally westward, but globally remain relatively untilted. Since individual spacecraft sample only one cut through the shock surface, accurate shock timing by several spacecraft would be required to differentiate between 'global' and 'local' shock tilts.

In this paper we have shown that the CMEs observed by Ulysses during its in-ecliptic passage to Jupiter were generally expanding and that the rate of expansion decreases with increasing heliocentric distance. Analysis of the shocks preceding these ejecta suggests that while the speed of the shocks (in the upstream frame of reference) decreases with increasing distance from the Sun, there is no discernible trend in shock strength. We suggest that the combination of decreasing shock speed, together with decreasing wave speed (in the upstream wind) moving away from the Sun is responsible for this result. We found that 12 out of 14 (86%) shock normals are tilted toward the equator in the meridional plane, and that 12 out of 14 (86%) shock normals are tilted toward the west in the azimuthal plane. The observed meridional tilts are consistent with simulations, suggesting that slow dense flow equatorward of the observations is responsible for 'refracting' the front normals toward the equator. Although several possible explanations for the azimuthal tilts were discussed, ultimately, their cause remains unknown.

Acknowledgments. We would like to thank D. Odstrčil, V. J. Pizzo, J. Americo González-Esparza, and Zoran Mikic for useful discussions. We are grateful to the referees for their comments and in particular to one of them for pointing out the relationship between dv/dt and R for ballistic expansion. This work was performed under the auspices of the U.S. Department of Energy with support from NASA. PR gratefully acknowledges the support of

the U.S. Department of Energy (subcontract G35240018-97), the National Aeronautics and Space Administration (NASW-98007 and NASW-98030), and the National Science Foundation (Space Weather Program ATM9613834).

References

Abraham-Shrauner, B., and S. H. Yun, Interplanetary shocks seen by Ames plasma probe on Pioneer 6 and 7, *J. Geophys. Res., 81,* 2097, 1976.

Balogh, A. T. J. Beek, R. J. Forsyth, P. C. Hedgecock, R. J. Marquedant, E. J. Smith, D. J. Southwood, and B. T. Tsurutani, The magnetic field investigation on the Ulysses mission: Instrumentation and preliminary scientific results, *Astron. and Astrophys., Suppl. Ser., 92,* 221, 1992.

Balogh, A., J. A. González-Esparza, R. J. Forsyth, M. E. Burton, B. E. Goldstein, E. J. Smith, and S. J. Bame, Interplanetary shock waves: Ulysses observations in and out of the ecliptic plane, in *The High Latitude Heliosphere, Proceedings of the 28th ESLAB Symposium,* pp. 171-180, editor R. G. Marsden, Kluwer Academic Publishers, 1995.

Bame, S. J., D. J. McComas, B. L. Barraclough, J. L. Phillips, K. J. Sofaly, J. C. Chavez, B. E. Goldstein, and R. K. Sakurai, The Ulysses solar wind plasma experiment, *Astron. and Astrophys., Suppl. Ser., 92,* 237, 1992.

Burton, M. E., E. J. Smith, B. E. Goldstein, A. Balogh, R. J. Forsyth, and S. J. Bame, Ulysses: Interplanetary shocks between 1 and 4 AU, *Geophys. Res. Lett., 19,* 1287, 1992.

González-Esparza, J. A., M. Neugebauer, E. J. Smith, and J. L. Phillips, Radial evolution of ejecta characteristics and transient shocks: Ulysses in-ecliptic observations, *J. Geophys. Res., 103,* 4767, 1998.

González-Esparza and S. Bravo, Two spacecraft observations of transient shocks and ejecta in the interplanetary medium, *J. Geophys. Res., 103,* 29,643, 1998.

Gosling, J. T., and P. Riley, The acceleration of slow coronal mass ejections in the high-speed solar wind, *J. Geophys. Res.*, 23, 2867, 1996.

Gosling, J. T., V. J. Pizzo, and S. J. Bame, Anomalously low proton temperatures in the solar wind following interplanetary shock waves: Evidence for magnetic bottles?, *J. Geophys. Res., 78,* 2001, 1973.

Gosling, J. T., M. F. Thomsen, S. J. Bame, and R. D. Zwickl, The eastward deflection of fast coronal mass ejecta in interplanetary space, *J. Geophys. Res., 92,* 12,399, 1987.

Gosling, J. T., S. J. Bame, D. J. McComas, J. L. Phillips, V. J. Pizzo, B.E. Goldstein, and M. Neugebauer, Solar wind corotating stream interaction regions out of the ecliptic plane: Ulysses, *Space Sci. Rev.*, *72*, 99, 1995a.

Gosling, J. T., D. J. McComas, J. L. Phillips, V. J. Pizzo, B.E. Goldstein, R. J. Forsyth, and R. P. Lepping, A CME-driven solar wind disturbance observed at both low and high heliographic latitudes, *Geophys. Res. Lett.*, *22*, 1753, 1995b.

Gosling, J. T., S. J. Bame, W. C. Feldman, D. J. McComas, P. Riley, B. E. Goldstein, and M. Neugebauer, The northern edge of the band of solar wind variability: Ulysses at ~ 4.5 AU, *Geophys. Res. Lett.*, *24*, 309, 1997.

Hirshberg, J., S. J. Bame, and D. E. Robbins, Solar flares and solar wind helium enrichments: July 1965–July 1967, *Sol. Phys.*, *23*, 467, 1972.

Hundhausen, A. J., Evolution of large–scale solar wind structures beyond 1 AU, *J. Geophys. Res.*, *78*, 2035, 1973.

Lanzerotti, L. J., C. G. Maclennan, R. E. Gold, S. E. Hawkins, III, S. J. Tappin, and R. J. Forsyth, Solar particle composition: Measurements in the March 1991 event at 2.5 AU, *Geophys. Res. Lett.*, *19*, 1251, 1992.

McComas, D. J., P. Riley, J. T. Gosling, A. Balogh, and R. J. Forsyth, Ulysses' rapid crossing of the polar coronal hole boundary, *J. Geophys. Res.*, *103*, 1955, 1998.

Odstrčil, D., M. Dryer, and Z. Smith, Propagation of an interplanetary shock wave along the heliospheric plasma sheet, *J. Geophys. Res.*, *101*, 19973, 1996.

Odstrčil, D., and V. J. Pizzo, Three–dimensional propagation of coronal mass ejections in a structured solar wind flow: 1. CME launched within the streamer belt, *J. Geophys. Res.*, *104*, 483, 1999a.

Odstrčil, D., and V. J. Pizzo, Three–dimensional propagation of coronal mass ejections in a structured solar wind flow: 2. CME launched adjacent to the streamer belt, *J. Geophys. Res.*, *104*, 493, 1999b.

Phillips, J. L., Coronal mass ejections encountered by the Ulysses spacecraft during the in-ecliptic mission phase, Unclassified Report 97–1086, Los Alamos Nat. Lab., Los Alamos, N. M., 1997.

Phillips, J. L., S. J. Bame, J. T. Gosling, D. J. McComas, B. E. Goldstein, E. J. Smith, A. Balogh, and R. J. Forsyth, Ulysses plasma observations of coronal mass ejections near 2.5 AU, *Geophys. Res. Lett.*, *19*, 1239, 1992.

Pizzo, V. J., An evaluation of corotating solar wind stream models, in *Solar Wind 5*, edited by H. Rosenbauer, published by Max-Planck-Institut fur Aeronomie, Katlenburg-Lindau, and Max-Planck-Institut fur extraterrestrische Physik, Garching, Germany, p. 153, 1981.

Riley, P. and J. T. Gosling, Do coronal mass ejections implode?, *Geophys. Res. Lett.*, *25*, 1529, 1998.

Riley, P., J. T. Gosling, L. A. Weiss, and V. J. Pizzo, The tilts of corotating interaction regions at midheliographic latitudes, *J. Geophys. Res.*, *101*, 24349, 1996.

Riley, P., J. T. Gosling, and V. J. Pizzo, A two-dimensional simulation of the radial and latitudinal evolution of a solar wind disturbance driven by a fast, high-pressure coronal mass ejection, *J. Geophys. Res.*, *102*, 14,677, 1997.

R. J. Forsyth, Space and Atmospheric Physics, The Blackett Laboratory, Imperial College, London SW7 2BZ, United Kingdom. (e-mail:r.forsyth@ic.ac.uk)

J. T. Gosling, D. J. McComas, Los Alamos National Laboratory, Los Alamos, NM 87545. (e-mail: jgosling@lanl.gov)

P. Riley, Science Applications International Corporation, San Diego, CA 92121. (e-mail:uk2@haven.saic.com)

Received N/A; revised N/A; accepted N/A.

Figure 1. Speed profiles for 17 CMEs. The first panel identifies the axes for each subsequent plot. Panels 2 and 3 (CMEs 1 and 2) show CMEs from 1990, panels 17 and 18 (CMEs 16 and 17) show CMEs from 1992, and the remaining panels show CMEs from 1991. The straight line in each panel is a least squares fit to the data. A negative slope indicates that the leading edge of the CME is traveling faster than the trailing edge, indicating that the CME is expanding.

Figure 2. (a) The expansion rate, defined as the negative of the slopes calculated from Figure 2, is plotted against heliocentric distance for the 14 CMEs that drove shocks. The dashed line is a least squares fit to the data. (b) Expansion rate multiplied by the heliocentric distance of the ejecta.

Figure 3. Shock speed relative to the upstream solar wind reference frame (v^*_{shock}) versus heliocentric distance for 14 fast-mode shocks.

Figure 4. (a) Shock strength (as inferred from the ratio of downstream density to upstream density minus one) versus distance from the Sun; (b) Ratio of downstream to upstream magnetic field strength; and (c) Magnetosonic Mach number.

Figure 5. (a) Sound speed ; (b) Alfvén speed; and (c) Magnetosonic speed immediately upstream of the shocks.

Figure 6. (a) Meridional tilt of shock normals (θ), and (b) azimuthal tilt of shock normals (ϕ) versus heliocentric distance.

Figure 7. (a) Solar wind speed, (b) number density, and (c) pressure profiles at 2 times (83 and 350 hours) following the launch of a pulse introduced at the inner boundary. The vertical lines mark the boundary of the pulse.

Table 1. CMEs observed by Ulysses during its in-ecliptic outward transit to Jupiter.

Start Date	Start Time	Stop Date	Stop Time	Shock?	Used in Current Study?
11/29/90	02:53	11/29/90	06:15	no	yes
12/01/90	04:25	12/01/90	12:30	no	yes
12/11/90	02:25	12/13/90	18:00	yes	no
12/26/90	15:30	12/28/90	11:40	yes	no
01/11/91	03:25	01/11/91	11:00	no	no
01/16/91	16:29	01/19/91	00:40	yes	yes
02/27/91	04:44	02/27/91	17:00	yes	yes
03/05/91	01:00	03/07/91	23:45	yes	yes
03/15/91	22:45	03/18/91	13:00	yes	yes
03/21/91	12:30	03/21/91	20:45	yes	yes
03/24/91	06:31	03/26/91	11:40	yes	no
03/27/91	09:15	03/29/91	12:00	yes	yes
03/29/91	12:00	04/02/91	18:45	no	no
04/08/91	16:10	04/11/91	15:05	yes	no
05/29/91	15:15	05/31/91	14:30	yes	yes
06/04/91	01:35	06/05/91	08:00	yes	yes
08/09/91	17:00	08/11/91	06:00-18:00	no	no
09/10/91	05:30	09/13/91	08:00	yes	yes
09/18/91	11:00	09/19/91	11:00	yes	yes
10/27/91	12:00	10/28/91	02:05	yes	yes

Table 1. (continued)

Start Date	Start Time	Stop Date	Stop Time	Shock?	Used in Current Study?
11/10/91	12:20	11/13/91	12:35	yes	no
11/17/91	15:00	11/20/91	14:00	no	yes
12/27/91	03:00	12/27/91	20:30	yes	yes
01/12/92	11:15	01/13/92	15:30	yes	yes
01/21/92	15:50	01/22/92	09:50	no	yes

Table 2. Shock parameters.

Year	DOY	Time	θ	ϕ	v_{shock}	v^{*}_{shock}	Υ	R (AU)
90	343	19:17	28.09	-24.18	417.78	122.36	0.76	1.347
90	358	16:00	-27.95	33.75	325.79	43.62	1.40	1.501
91	014	07:55	21.00	40.10	348.02	67.57	0.79	1.728
91	062	23:49	40.58	2.57	469.01	120.42	0.37	2.266
91	078	22:25	18.31	28.85	471.84	90.38	0.80	2.438
91	082	15:40	21.31	53.34	328.94	93.87	3.22	2.479
91	097	04:46	36.29	9.45	470.92	116.02	2.88	2.633
91	154	17:06	-3.89	35.09	432.32	71.83	2.25	3.219
91	251	08:27	43.82	28.27	316.64	28.93	0.71	4.117
91	261	07:10	35.34	-2.62	377.34	50.91	0.67	4.204
91	299	22:03	42.63	20.46	361.00	62.19	2.37	4.535
91	313	08:21	1.78	13.68	437.74	47.20	2.41	4.646
91	360	19:45	36.71	40.40	303.42	30.87	1.76	5.033
92	012	04:00	0.71	59.79	313.30	23.11	0.44	5.162

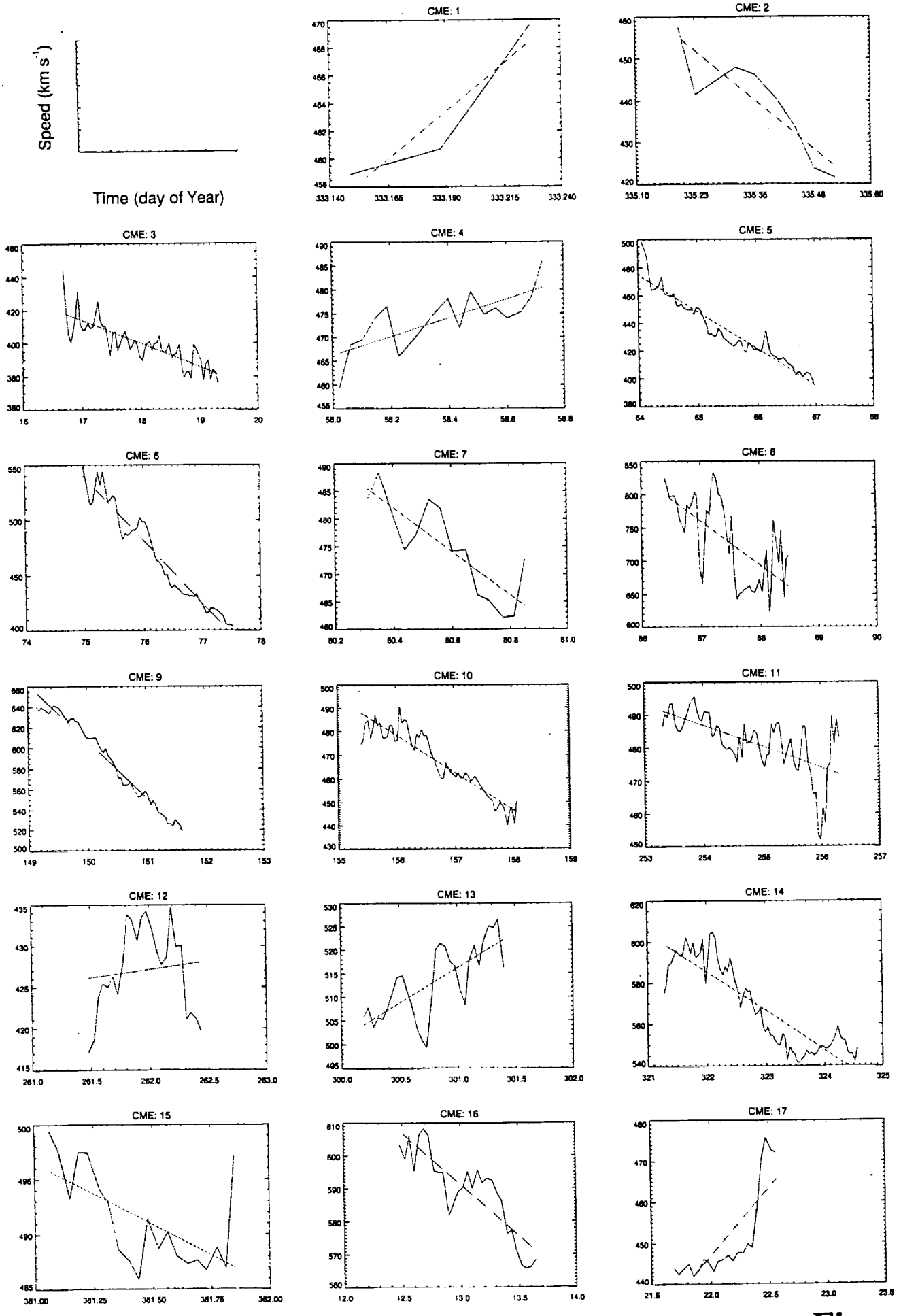
Speed (km s^{-1})
Time (day of Year)
CME: 1
CME: 2
CME: 3
CME: 4
CME: 5
CME: 6
CME: 7
CME: 8
CME: 9
CME: 10
CME: 11
CME: 12
CME: 13
CME: 14
CME: 15
CME: 16
CME: 17

Figure 1

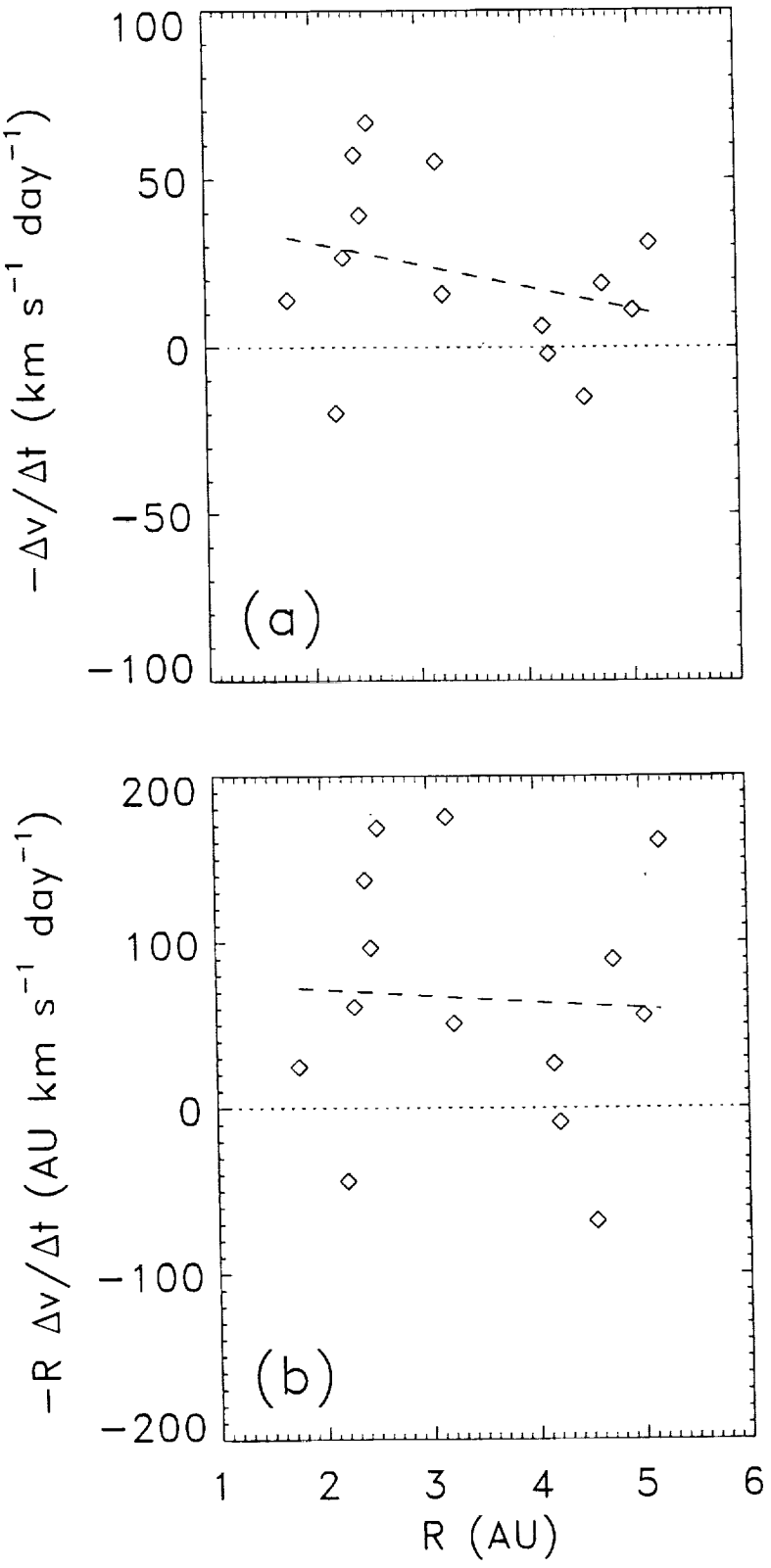
100
50
0
−50
−100
−Δv/Δt (km s^{-1} day^{-1})
(a)
200
100
0
−100
−200
−R Δv/Δt (AU km s^{-1} day^{-1})
(b)
1
2
3
4
5
6
R (AU)

Figure 2

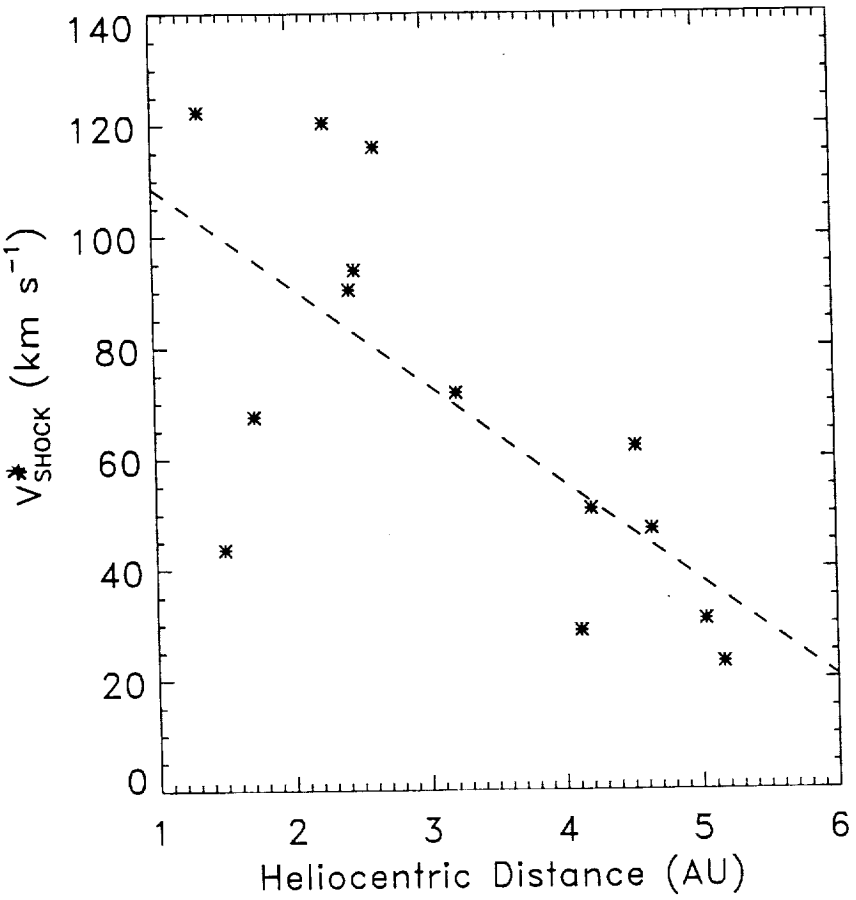
140
120
100
80
60
40
20
0
V_{SHOCK} (km s^{-1})
1
2
3
4
5
6
Heliocentric Distance (AU)

Figure 3

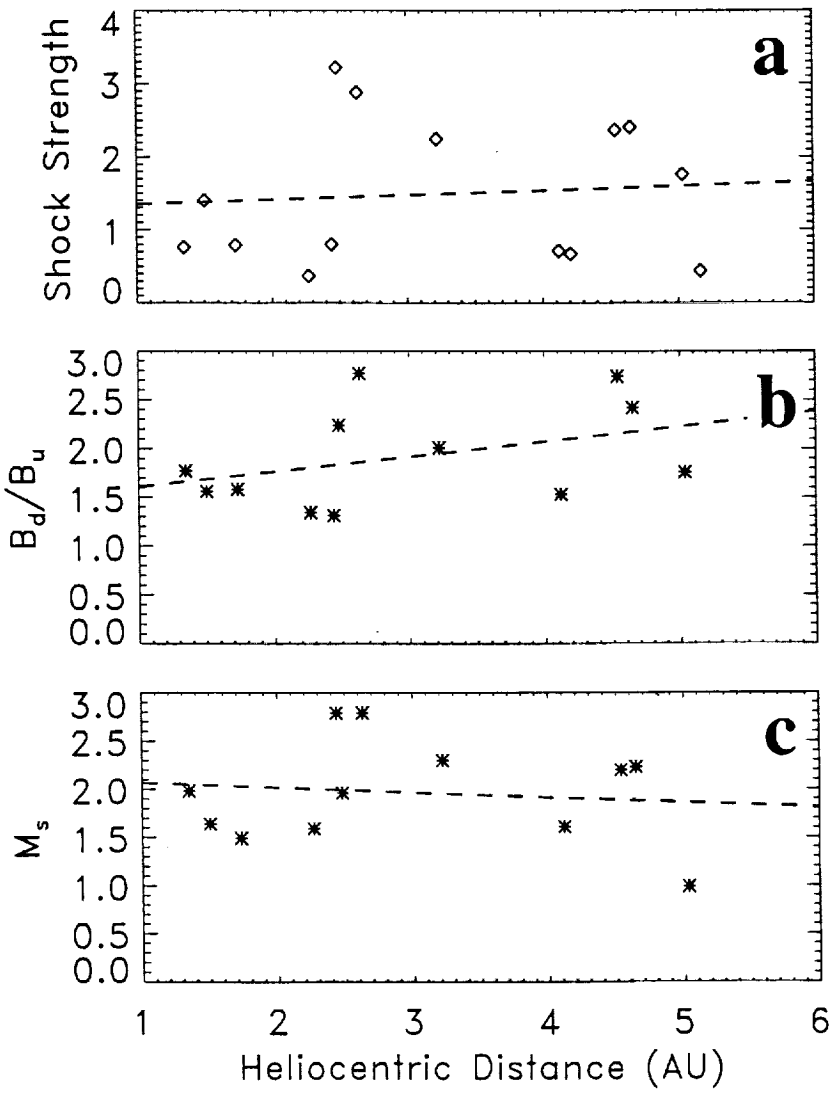
a
Shock Strength
0
1
2
3
4
b
B_d/B_u
0.0
0.5
1.0
1.5
2.0
2.5
3.0
c
M_s
0.0
0.5
1.0
1.5
2.0
2.5
3.0
1
2
3
4
5
6
Heliocentric Distance (AU)

Figure 4

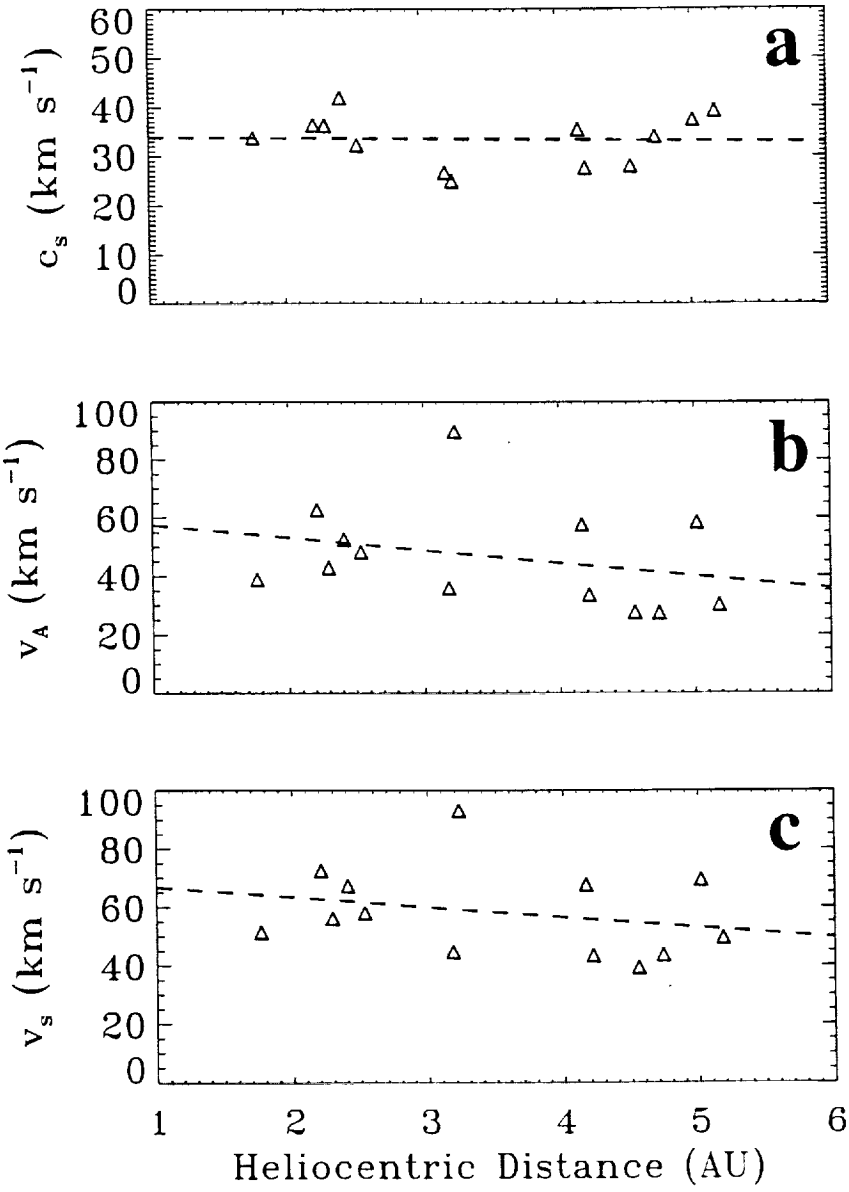
a
b
c
c_s (km s^{-1})
v_A (km s^{-1})
v_s (km s^{-1})
0
10
20
30
40
50
60
80
100
1
2
3
4
5
6
Heliocentric Distance (AU)

Figure 5

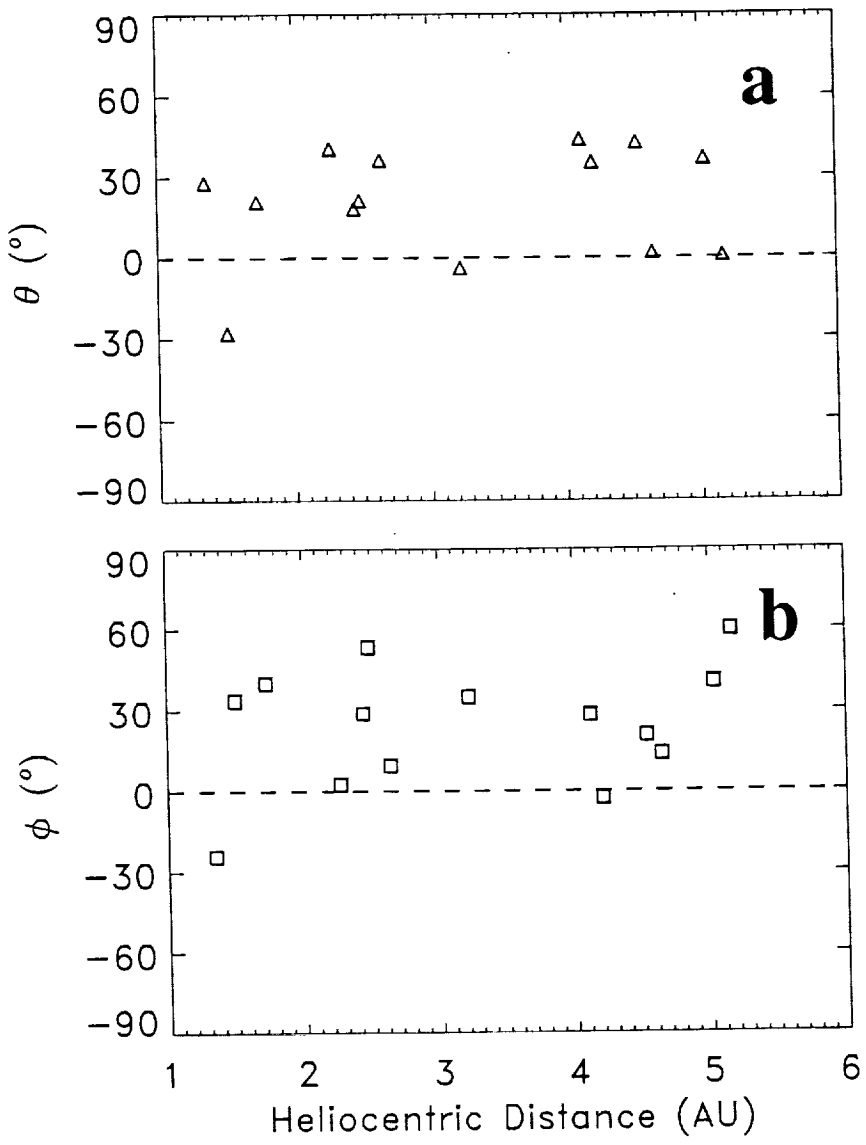

Figure 6

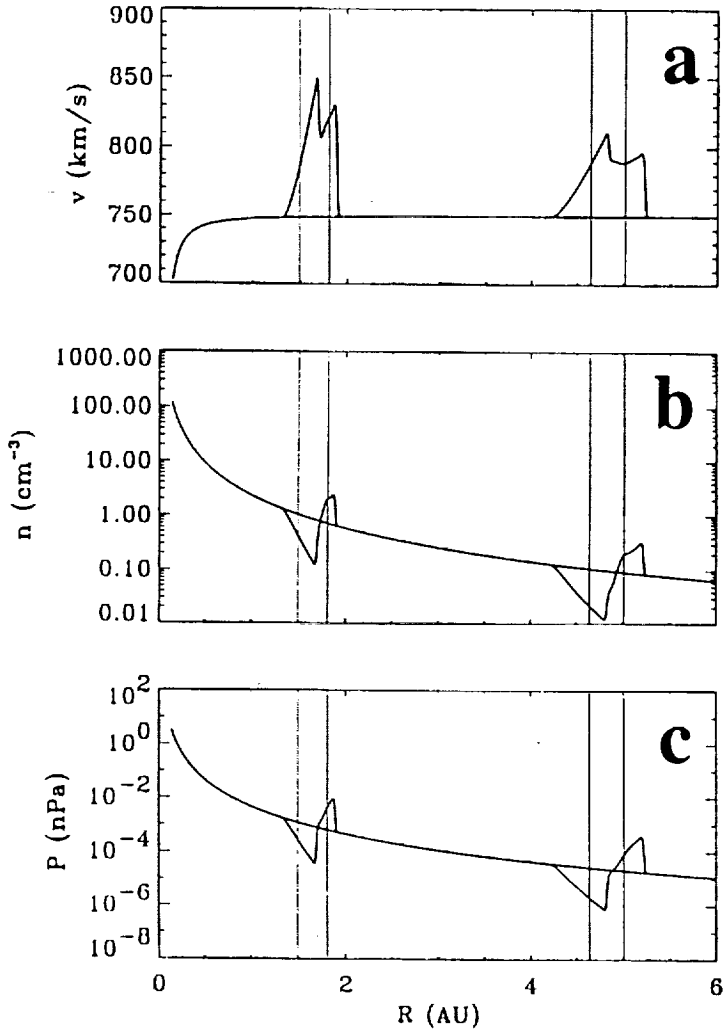
a
b
c
v (km/s)
900
850
800
750
700
n (cm^{-3})
1000.00
100.00
10.00
1.00
0.10
0.01
P (nPa)
10^{2}
10^{0}
10^{-2}
10^{-4}
10^{-6}
10^{-8}
0
2
4
6
R (AU)

Figure 7

Appendix 2

Fluid aspects of solar wind disturbances driven by coronal mass ejections

J. T. Gosling and Pete Riley

Submitted to the *Journal of Geophysical Research*, December, 1999.

LA-UR- 99-5887

Approved for public release; distribution is unlimited.

Title: FLUID ASPECTS OF SOLAR WIND DISTURBANCES DRIVEN BY CORONAL MASS EJECTIONS

Author(s): John T. Gosling, NIS-1
Pete Riley, SAIC, San Diego, California

Submitted to: Journal of Geophysical Research

Los Alamos
NATIONAL LABORATORY

Fluid Aspects of Solar Wind Disturbances Driven by Coronal Mass Ejections

J. T. Gosling
Los Alamos National Laboratory
Los Alamos, New Mexico

Pete Riley
SAIC
San Diego, California

Abstract. Transient solar wind disturbances are largely associated with coronal mass ejections (CMEs). Such disturbances often produce large geomagnetic storms, gradual solar energetic particle events, and Forbush Decreases in the galactic cosmic ray intensity. This paper provides an overview of fluid aspects important in the evolution of these disturbances as they propagate out through the heliosphere. The intent is to illustrate the prime dynamic processes that govern disturbance evolution in the solar wind and to explore how different types of initial conditions, both within the CMEs themselves and within the ambient wind, affect disturbance evolution. The overview proceeds from simple one-dimensional simulations of the effects of simple speed perturbations propagating into a structureless solar wind to three-dimensional simulations that consider effects associated with compound speed and pressure perturbations propagating into a spatially structured solar wind.

Introduction

The most dramatic temporal changes in the coronal expansion occur during coronal mass ejection (CME) events, during which somewhere between 10^{15} and 10^{16} g of solar material are injected into the solar wind [e.g., *Crooker, Joselyn, and Feynman*, 1997; *Gosling*, 1999; *Hundhausen*, 1997]. These events originate in closed magnetic field regions in the solar atmosphere not previously participating in the solar wind expansion. Ejection speeds within about 5 solar radii of the Sun's surface range from less than 50 km s^{-1} in some of the slower events to as high as 2000

km s^{-1} in some of the faster events [e.g., *Gosling et al.*, 1976; *Hundhausen et al.*, 1994; *Sheeley et al.*, 1999]. Many CMEs have outward speeds and internal plasma and magnetic field pressures that are quite different from that of the ambient wind into which they are injected. Such CMEs produce transient disturbances in the solar wind that should propagate to the far reaches of the heliosphere.

Transient disturbances in the solar wind initiated by coronal eruptions have been modeled for many years, beginning with the self-similar analytical models of *Parker* [1961; 1963] and *Simon and Axford* [1966]. The first numerical computer code (one-dimensional, gas dynamic) to study disturbance propagation in the solar wind was developed in the late 1960s [*Hundhausen and Gentry*, 1969], and a variety of other codes ranging from simple one-dimensional gas dynamic codes through three-dimensional gas dynamic and magnetohydrodynamic codes have been developed in subsequent years. For the most part, these codes have been applied to the problem of disturbances driven by fast CMEs propagating into a structureless solar wind. *Pizzo* [1985] provided an excellent summary of the level of understanding achieved from such simulation studies through about 1984, and other reviews have subsequently become available [e.g., *Dryer*, 1994; *Pizzo*, 1997; *Riley*, 1999]. More recently, some attention has been focused on disturbances generated by slow CMEs [e.g., *Gosling and Riley*, 1996], on disturbances driven by CMEs having high internal pressures [e.g., *Gosling et al.*, 1994a; 1994b; 1998; *Riley and Gosling*, 1998], and disturbance propagation effects associated with a structured ambient solar wind [e.g., *Odstrcil et al.*, 1996; 1999a; 1999b; *Riley et al.*, 1997].

Our purpose here is to provide a brief tutorial on fluid aspects of solar wind disturbances derived from numerical gas dynamic simulations. For the most part we illustrate disturbance evolution by propagating idealized perturbations, mimicking different types of CMEs, into a structureless solar wind using a simple one-dimensional, adiabatic (except at shocks), gas dynamic code. The simulations begin outside the critical point where the solar wind becomes supersonic and thus do not address questions of how the CMEs themselves are initiated. Limited to one dimension (the radial direction), the simulation code predicts too strong an interaction between newly ejected solar material and the ambient wind because it neglects azimuthal and meridional motions of the plasma that help relieve pressure stresses. Moreover, the code ignores magnetic forces and thus also underestimates the speed with which pressure disturbances propagate in the wind. Despite these

limitations, calculations using this code provide an excellent starting point for illustrating and understanding how solar wind disturbances associated with CMEs evolve with increasing heliocentric distance. Our intent is to illustrate (1) the primary fluid processes that determine disturbance evolution and (2) the effect that initial conditions, both in the ambient wind and within the CMEs themselves, have on disturbance dynamics. This tutorial builds on and extends to different types of disturbances a tutorial by *Hundhausen* [1985], who used a similar one-dimensional fluid code to illustrate fluid aspects of solar wind disturbances initiated by fast CMEs. We refer the interested reader to that paper for an informative discussion of simulations of this nature. In the latter part of this paper we illustrate some of the additional effects that arise in solar wind disturbances due to structure in the ambient wind and transverse (to the radial) flows, as revealed by multidimensional simulations.

Formation and Propagation of Compressions and Rarefactions.

Spatial and temporal gradients in flow speed lead to the formation of compressions and rarefactions that propagate through and modify the structure of the solar wind. We begin our discussion of fluid aspects of disturbance evolution in the solar wind by considering the dynamic evolution of compressions and rarefactions generated by step-like changes in speed close to the Sun. In all of the simulations discussed here the flow speed, plasma density, and pressure are first held constant at the inner boundary of the simulation at 0.14 AU (30 solar radii) for a sufficiently long time that a steady, highly supersonic solar wind expansion fills the computational mesh. Different types of simple perturbations are then introduced at the inner boundary. In the example shown in Figure 1 the initial steady state expansion produced an asymptotic solar wind speed of about 480 km s^{-1} at large heliocentric distances. The figure shows two superimposed snapshots of the radial evolution of a disturbance initiated by discontinuously increasing the flow speed from 400 to 700 km s^{-1} at the inner boundary while simultaneously holding the density and pressure constant. A high-pressure compression region, which expands both forward into the slow wind and backward into the fast wind, quickly forms as the faster plasma overtakes the slower wind ahead. In this case, the compression is bounded by a strong forward-reverse shock pair since the plasma flows supersonically into the compression from both sides. The slower

plasma is compressed and accelerated as it encounters the forward shock and the faster wind is compressed and decelerated as it encounters the reverse shock. The vertical lines in Figure 1 bracket the last 30 hours of slow wind introduced at the inner boundary. This plasma parcel is compressed into an ever smaller volume as the forward shock passes through it. When the fast and slow plasmas have equal densities at the inner boundary, as in this example, momentum conservation dictates that a step function increase in speed produces nearly equal and opposite speed changes in the slow and fast wind. (The changes would be precisely equal and opposite were it not for the overall R^{-2} fall off in density, where R is heliocentric distance.) Essentially the same result is obtained if the speed increase at the inner boundary is more gradual than a step function, but the interaction develops more slowly and the shocks form farther from the Sun.

Figure 2 shows two superimposed snapshots illustrating the radial evolution of a disturbance initiated at the inner boundary in the opposite manner from that in Figure 1. In this case the steady state expansion produced an asymptotic flow speed at large distances of about 750 km s^{-1}. The disturbance was initiated by changing the speed at the inner boundary from 700 to 400 km s^{-1} in a step function decrease while holding the density and pressure constant there. A region of low pressure quickly forms at the interface between the two flows as the faster plasma runs away from the slower. This region of low pressure is commonly called a rarefaction (our preference) or an expansion wave. The slower plasma behind the interface is accelerated as it encounters the enhanced outward pressure gradient associated with the rarefaction, while the faster plasma ahead of the interface is decelerated by the reverse pressure gradient associated with the leading portion of the rarefaction. It is of interest that the rarefaction in Figure 2 expands much more quickly than does the compression in Figure 1 because it is superimposed upon diverging flows. With increasing heliocentric distance, the overall speed profile flattens as the rarefaction spreads into the surrounding plasma. Vertical lines in the figure bracket the first 30 hours of slow plasma introduced at the inner boundary. This parcel of plasma broadens as it moves out from the Sun and eventually all of the plasma within the parcel is accelerated to a higher speed as it encounters the low-pressure rarefaction. The greatest acceleration is experienced by the plasma at the leading edge of the parcel; however, the change in speed of the leading edge of the parcel remains less than half the original difference in speed between the fast and slow flows because of momentum conservation in a plasma whose overall density varies as R^{-2}. The spherical nature of the overall

solar wind expansion is also the reason why the pressure perturbation associated with the rarefaction is asymmetric about the interface, with the pressure minimum migrating into the plasma ahead of the parcel as the disturbance progresses out into the heliosphere.

Disturbances Produced by Fast CMEs

Figure 3 shows three superimposed snapshots of the radial evolution of a disturbance initiated by combining the above types of speed changes in a square wave increase in speed. In this case speed, density, and pressure were first held steady at the inner boundary at 0.14 AU until a stationary flow with an asymptotic speed of ~450 km s^{-1} filled the computational mesh. The disturbance was initiated at the inner boundary by raising the flow speed from 350 to 600 km s^{-1} and then dropping it back to 350 km s^{-1} 15 hours later. The initial disturbance mimics a moderately fast CME injected into a considerably slower wind and having an internal pressure equal to that of the ambient wind. As would be expected from Figure 1, a region of high pressure develops on the leading edge of the CME in the simulation as it runs into the slower ambient wind ahead. Because of the large amplitude of the initial speed perturbation, this region of high pressure is bounded by a forward-reverse shock pair. The propagation of these shocks produces an acceleration of the ambient wind ahead and a deceleration of the leading portion of the CME.

Simultaneously, a rarefaction develops on the trailing edge of the disturbance as the CME pulls away from slower trailing solar wind. Pressure gradients associated with this rarefaction produce a deceleration of the trailing portion of the CME and an acceleration of the trailing wind. After 69 hours the reverse shock and the leading edge of the rarefaction have propagated through one another in opposite directions, with the reverse shock being near the middle of the CME and the leading edge of the rarefaction being close to the front edge of the CME. The back edge of the rarefaction is now well into the trailing wind behind the CME (the back edge of the disturbance at 69 hours lies close to the position of the front edge of the disturbance at 27 hours). After 125 hours the reverse shock has propagated almost to the back edge of the CME, while the leading edge of the rarefaction has propagated almost up to the forward shock ahead of the CME. The disturbance thus evolves from an initial, limited square wave perturbation in speed into a more complex disturbance with an overall speed profile that resembles a double sawtooth. As a result of

sharing its momentum with both the leading and the trailing ambient wind via the compression and rarefaction waves, the CME slows considerably as it propagates out into the heliosphere. The simulation thus explains why CMEs with speeds considerably higher than that of the normal wind are only occasionally observed far from the Sun. Only those CMEs with exceptionally large inertia will not be slowed substantially as they interact with a slower ambient solar wind. Finally, although the simulated CME was not expanding at the inner boundary and has a radial width near 1.7 AU that is comparable to its width (0.22 AU) at the inner boundary, it does expand once the reverse wave has passed through its back edge. When the perturbation at the inner boundary is of shorter duration than in the present example, the reverse wave passes more quickly through the CME and expansion begins sooner. The simple simulation shown in Figure 3 is qualitatively consistent with near-ecliptic observations of many CME-driven solar wind disturbances, although reverse shocks are only rarely detected in these disturbances except possibly along their central axes [e.g., *Gosling et al.*, 1988] where the interaction is most nearly one-dimensional in nature.

Disturbances Produced by Slow CMEs

It is instructive to consider the inverse problem of a slow CME injected into a much faster surrounding solar wind such as might happen at high latitudes. Figure 4 shows two superimposed snapshots of calculated radial speed and pressure profiles of a solar wind disturbance produced in our one-dimensional simulation by introducing a very slow pulse into a faster ambient wind. Starting with the same steady state solution as in Figure 3, the disturbance is initiated at the inner boundary by dropping the flow speed from 350 to 200 km s^{-1} and then raising it back up to 350 km s^{-1} in a square wave pulse 15-hours long. Because of the speed gradient at the leading edge of the CME, a rarefaction quickly forms there that rapidly spreads forward into the ambient wind and back through the CME. Simultaneously a compression region, which is bounded by a forward-reverse shock pair, forms on the trailing edge of the CME as the faster trailing wind overtakes the CME. After 41 hours the forward shock and the trailing edge of the rarefaction have passed through one another in opposite directions such that the forward shock lies within the heart of the CME while the rarefaction extends nearly to its back edge. After 111 hours the rarefaction extends well behind the CME but still leads the reverse shock, while the

forward shock has propagated entirely through the CME. Meanwhile the leading edge of the rarefaction has run well ahead of both the CME and the forward shock. The combined effect of the shocks and the rarefaction wave produces a compressed CME that, at 1 AU, is traveling almost at the speed of the ambient wind as yet unaffected by the the disturbance. Indeed at this distance the entire CME is traveling faster than the decelerated ambient wind immediately ahead of the forward shock. An untrained observer might mistakenly believe that the forward-reverse shock pair was driven by a CME that initially had a higher speed than that of the ambient wind ahead rather than a lower speed.

The simulation shown in Figure 4 demonstrates that if a slow CME is inserted into a faster solar wind it is rapidly accelerated up to nearly the speed of the surrounding wind [*Gosling and Riley*, 1996]. The low momentum of the CME in this case is rapidly shared with an ever larger volume of the ambient wind owing to the propagation of the compression and rarefaction waves. The forward shock and the leading rarefaction persist to large distances and thus provide telltale evidence of the acceleration process. Observations, particularly in the outer heliosphere and at high heliographic latitudes, provide a few relatively dramatic examples where CMEs have been accelerated to higher speed because of interactions of this sort, although those observations can not be explained in terms of simple square wave inputs such as specifically simulated here. Moreover, most slow CMEs observed in the ecliptic plane do not appear to have been accelerated substantially by this kind of interaction since they are typically not associated with large rarefactions or shocks [*Gosling*, 1994]. Both *in situ* and coronal [e.g., *Sheeley*, 1999] observations indicate that virtually all low-speed CMEs in the solar wind are accelerated outward by pressure gradients similar to those that accelerate the normal slow solar wind.

Disturbances Produced by the Overexpansion of CMEs

Coronagraph observations reveal that most CMEs expand considerably as they propagate away from the Sun, quickly becoming much larger than the Sun that spawned them. For most CMEs this expansion continues far out into the heliosphere and is readily evident by the fact that the leading edges of most CMEs observed in the solar wind at any heliocentric distance have higher speeds than the trailing edges. Since the expansion occurs in all three dimensions, the density and

temperature of the plasma within a CME typically decrease with increasing heliocentric distance more rapidly than does that of the normal solar wind. Thus, at 1 AU CMEs in the solar wind often are characterized by anomalously low kinetic temperatures [e.g., *Gosling et al.*, 1973; 1987; *Montgomery et al.*, 1974; *Richardson and Cane*, 1995], and, at distances beyond about 3 AU, by unusually low plasma densities as well [*Gosling et al.*, 1998].

Several processes can contribute to the expansion of a CME. A CME can expand simply because it is injected into the solar wind with a substantial front-to-rear speed gradient. Another possibility is that expansion is a CME's response to a rarefaction wave produced by relative motion between the CME and the surrounding solar wind, as discussed above. Finally, a CME may expand because it has a higher internal pressure than that of the surrounding solar wind. The higher pressure can be a result of a higher density, a higher temperature, a stronger magnetic field, or some combination thereof. We have used the term "overexpansion" to describe CME events where a higher internal pressure contributes substantially to the expansion. The relative importance of these various expansion processes differs from event to event, depending on the physical character of the CME and on initial conditions within the surrounding solar wind.

Figure 5 show snapshots of solar wind speed and pressure as a function of heliocentric distance obtained in a simulation of an overexpanding CME. In this case the initial steady state boundary conditions produced a highly supersonic flow with a speed of 750 km s^{-1} at 6.0 AU and a density of 2.5 cm^{-3} at 1 AU, matching average high-latitude flow conditions observed by Ulysses on the declining phase of the last solar cycle [e.g., *Phillips et al.*, 1995]. The disturbance was initiated at the inner boundary by increasing the density (and hence also the pressure) by a factor of four in a bell-shaped pulse 10-hours long while simultaneously holding the temperature and speed constant. This mimics the injection of a dense CME into the heliosphere whose internal pressure is higher than that of the surrounding wind and whose speed is the same. The temporal duration of the initial pulse corresponds to a radial width of 0.17 AU at the inner boundary.

Because of its initial high internal pressure, the CME expands as it travels out from the Sun so that at 3.2 AU it has a radial width of 0.40 AU. The overall disturbance width at this distance is 0.67 AU since the expansion drives a forward compression wave into the ambient wind ahead and a reverse compression wave into the trailing wind. These pressure waves steepen into relatively weak shocks by the time they reach 3.2 AU. The expansion also produces a declining front-to-

rear speed gradient across the CME and causes the pressure within the CME far from the Sun to be lower than that in the ambient wind surrounding the disturbance. The disturbance thus evolves from one where high pressure is concentrated within the CME to one where high pressure is concentrated in the regions immediately downstream from the shocks and where the region interior to the CME has lower than average pressure. (Disturbance evolution is similar to this if the initial pressure enhancement is instead caused by a higher temperature or a stronger magnetic field, although differences in detail arise because of the different masses in the initial perturbations.) Since the background pressure continues to decrease with increasing heliocentric distance in the simulation, the CME continues to expand as it travels into the far reaches of the heliosphere [*Riley and Gosling*, 1998]. This conclusion would be modified if the addition of interstellar pickup ions into the solar wind contributes substantially to the background pressure at large distances. Insofar as we are aware, events such as this have not been identified at low heliographic latitudes at any heliocentric distance. On the other hand, events of this nature constituted a large fraction of the CME-related events observed at high heliographic latitudes by Ulysses during the decline and near the minimum of solar cycle 22. In particular, the disturbance produced by the simple simulation in Figure 5 closely resembles solar wind disturbances observed by Ulysses in February 1994 at 3.5 AU and S54° and in April 1994 at 3.2 AU and S61° [*Gosling et al.*, 1994b].

Disturbances Produced by Compound Perturbations

The simulation results shown in Figures 3-5 illustrate the simplest types of fluid interactions that occur between CMEs and the surrounding solar wind as they evolve outward from the Sun. Additional complexities arise when a CME provides both a speed and a pressure perturbation to the ambient wind. Figure 6 illustrates some of this additional complexity by introducing different types of perturbations into the same steady state flow (~430 km s^{-1} at large heliocentric distances). The disturbance on the left was initiated in the same manner as the one in Figure 5, albeit into lower speed ambient wind, by increasing the density at the inner boundary by a factor of four in a bell-shaped pulse 10-hours long while holding the temperature and speed constant. The overexpansion of this pressure pulse produces the speed and pressure profiles shown 59.1 hours after initiation at the inner boundary. In contrast, the disturbance shown in the middle of Figure 6

was initiated by increasing the flow speed by a factor of two in a bell-shaped pulse, also 10-hours long, while holding the density and pressure constant. This disturbance evolves much the same as the one shown in Figure 3, although differences arise because of the shorter and more gradual nature of the initial perturbation at the inner boundary when compared to the example in Figure 3.

Finally, the disturbance shown at the right in Figure 6 was initiated by combining these perturbations in a single pulse. That is, the disturbance was initiated at the inner boundary by simultaneously increasing both the speed (by a factor of two) and the density (by a factor of four) in a bell-shaped pulse 10-hours long while holding the temperature constant. This input mimics the injection of a moderately fast, high pressure CME into a slower ambient solar wind. We note that the resulting disturbance near 1 AU includes only a single forward-reverse shock pair. Primarily because of the greater initial momentum of the CME in this simulation, the forward shock near 1 AU is considerably stronger than in the example shown in the middle of the figure, and the CME slows less rapidly as it travels out from the Sun. After 59.1 hours the CME is also broader than the disturbances in the other panels because both the trailing rarefaction and the initial over pressure contribute to the expansion. The reverse shock in this simulation is associated with expansion of the compression region on the leading edge of the CME. It is weakened and retarded considerably as it encounters the forward wave associated with CME overexpansion. The weaker forward expansion wave is nearly obliterated by that interaction. On the other hand, the reverse compression wave associated with overexpansion of the CME never really develops fully in this case because the CME runs away from the trailing plasma faster than the reverse wave can effectively expand back into it. Overall, the disturbance bears a greater resemblance to the example driven by a pure speed pulse (middle panel) than that driven by a pure pressure pulse (left panel). This simulation thus illustrates the dominant role that relative speed plays in the evolution of most CME-driven solar wind disturbances.

Figure 7 provides a somewhat similar comparison for the case of slow CMEs injected into a much faster ambient solar wind flow (asymptotic speed of 750 km s^{-1} in this case). The disturbance in the left panel was initiated by dropping the speed from 700 to 400 km s^{-1} at the inner boundary and then raising it back up to 700 km s^{-1} in a bell-shaped pulse 30-hours long. In this case the outer edges of the simulated CME have the same high speed as the ambient wind, while the central portion of the CME has a much lower speed. Because of the more gradual nature

of the initial perturbation, its greater duration, and the fact that it is superimposed upon a much faster ambient wind, this disturbance evolves more slowly with heliocentric distance than does the square-wave example shown in Figure 4 . Nevertheless, the development of the rarefaction on the leading edge of the disturbance and the compression on the trailing edge of the disturbance are clear. Moreover, the CME is accelerated in much the same manner as in the Figure 4 example. By 4 AU, all portions of the simulated CME have speeds greater than 650 km s^{-1} as a result of momentum sharing with the surrounding wind, whereas the CME would have a minimum speed of ~480 km s^{-1} at large heliocentric distances in the absence of the dynamic interaction. Different choices for the edges of the CME within the original negative speed pulse would not alter this conclusion.

The disturbance in the right panel of Figure 7 was initiated at the inner boundary of the simulation by decreasing the speed in the same manner as in the left panel while simultaneously increasing the density by a factor of four in a bell-shaped pulse 30-hours long. When compared to the disturbance in the left panel, it is clear that the effect of adding the density/pressure perturbation is to broaden both the CME and the overall disturbance, to weaken the forward shock and retard its advance into the CME, to strengthen the reverse shock propagating back into the trailing ambient wind, and to lessen the overall acceleration of the CME. All of these effects are consequences of the added inertia of the initial perturbation and the additional expansion provided by the high initial internal pressure. Once again it is notable that expansion shocks, such as those produced when pure pressure signals of this same amplitude are introduced at the inner boundary (see Figure 5 and the left panel of Figure 6), do not form in this example. The reverse wave associated with expansion of the high-pressure CME is effectively obliterated as it interacts with and retards the forward shock associated with the compression on the trailing edge of the disturbance, while the forward expansion wave never really develops because the ambient wind ahead runs away from the CME faster than the CME can expand into it. The two examples shown in Figure 7 again illustrate the dominant role that relative speed plays in the evolution of most solar wind disturbances. The resulting disturbance in the right panel resembles a disturbance observed by Ulysses at 4.5 AU and S35° in July, 1993 [*Gosling and Riley*, 1996].

Disturbance Propagation Effects Associated With Latitudinal Structure in the Ambient Solar Wind

The examples shown in Figures 1-7 illustrate most of the basic fluid effects underlying CME-driven disturbance evolution in the solar wind. They also illustrate the sensitivity of that evolution to initial conditions and provide considerable guidance for interpreting observations. Real solar wind disturbances are, of course, often more complex than those illustrated by these simple simulations. Because of spatial structure within the ambient solar wind and within the CMEs themselves, as well as the possibility of transverse flows, we can not hope to replicate all the details of these disturbances with one-dimensional simulations. Additional effects arise when one considers spatial inhomogenieties and allows for transverse flow in the simulations. Figure 8 provides an example of some of these effects [*Riley et al.*, 1997]. The figure shows the result of a two-dimensional fluid simulation of a CME propagating into a solar wind characterized by dense, slow radial flow from the equator to a latitude of 20° and by tenuous, fast radial flow above 20°. At large heliocentric distances the steady state flow prior to initiation of the disturbance was ~450 km s^{-1} at low latitudes and ~750 km s^{-1} at high latitudes. This approximates the average latitudinal structure observed by Ulysses during its first polar orbit about the Sun on the declining phase of solar cycle 22 [e.g., *Phillips et al.*, 1995]. It represents the limiting case of a three-dimensional model in which the ambient flow close to the Sun is structured into a band of low-speed wind above the magnetic equator and a considerably higher-speed wind at higher magnetic latitudes. In this case the tilt of the solar magnetic dipole relative to the rotation axis of the Sun is exactly zero so that there is no stream structure at low or high heliographic latitudes and thus corotating interaction regions (CIRs) do not form.

The disturbance shown in Figure 8 was initiated at 0.14 AU by introducing a fast, hot and dense bell-shaped pulse of 10-hour duration into the simulation. The pulse extended from the equator to 45° latitude, extending well across the boundary between the low and high-latitude flows. The speed of the plasma in the pulse at all latitudes was identical to that in the ambient wind at high latitudes and the maximum gas pressure within the pulse was 6 times greater than that which prevailed at both low and high latitudes in the ambient wind. The simulation thus mimics injection into the solar wind of a CME that initially has a speed equal to that of the ambient wind at high

latitudes, a speed considerably faster than the ambient wind at low latitudes, and a higher internal pressure than the ambient wind at all latitudes. The upper portion of Figure 8 shows snapshots of the radial and meridional flows and the pressure 6.9 days after initiation of the disturbance at the inner boundary, while the bottom portion shows differences between the disturbance and steady state solutions of these parameters. The solid line in all panels outlines the material introduced within the pulse at the inner boundary and thus outlines the pseudo-CME in the simulation. The following items are of interest here:

1. The disturbance has evolved in a completely different fashion within the low and high-latitude regions. At low latitudes, evolution is dominated by the relative speed between the CME and the slower ambient wind ahead, as in the one-dimensional example in the right panel of Figure 6. As in that case, the low-latitude portion of the disturbance is fronted by a strong forward shock, while the reverse wave associated with the interaction is almost invisible. At high latitudes, disturbance evolution is driven primarily by the overexpansion of the coasting CME, as in Figure 5, and a relatively weak forward-reverse shock pair bounds the disturbance.

2. The CME has essentially separated into two pieces. The radial separation is caused by the strong velocity shear between the slow and fast ambient solar wind. The latitudinal separation is a result of the rarefactions that develop in the two different pieces of the CME. Pressure gradients associated with those rarefactions drive meridional flows across the original interface between the low and high-speed flows; those flows produce the latitudinal separation. The rarefaction at low latitudes is a result of the CME running away from the slower ambient behind (as in Figure 3 and in the middle and right panels in Figure 6). At high latitudes the rarefaction is the result of the overexpansion of the CME (as in Figure 5 and the left panel in Figure 6).

3. After 6.9 days the CME, originally confined to latitudes below 45°, extends poleward to 63° and the associated forward and reverse shocks have reached the pole. Most of this latitudinal expansion occurs close to the Sun where, because of the diverging geometry, latitudinal distances are relatively small. This poleward expansion is not yet obvious in high-latitude observations obtained to date.

4. The high-pressure region at the front of the low-latitude portion of the disturbance extends poleward across the slow/fast interface by ~10°. This extension is a result of the transverse expansion of the compression region and is associated with the strongest meridional flow

velocities (50 km s^{-1}) within the disturbance.

The disturbance profiles produced in this two-dimensional simulation at high and low latitudes are similar to disturbance profiles observed in the ecliptic plane at 1 AU by IMP 8 and at S54° and 3.5 AU by Ulysses during a CME-driven disturbance in February 1994 [*Gosling et al.*, 1995]. Although the two-dimensional simulation introduces additional complexities and provides a global perspective not possible in the one-dimensional simulations, the basic nature of the disturbances at high and low latitudes is correctly inferred from the simpler one-dimensional simulations.

Disturbance Propagation in a More Realistic Three-Dimensional Geometry

The geometry of the ambient solar wind flow close to the Sun is probably never as simple as assumed in Figure 8. Stream structure and CIRs always are present to some degree in the solar wind at low heliographic latitudes. A more realistic, but still highly idealized, geometry is that which has been used to simulate three-dimensional aspects of CIRs [*Pizzo*, 1991; 1994; *Pizzo and Gosling*, 1994]. In those simulations it is assumed that a uniform band of slow, dense wind encircles the Sun at low heliographic latitudes, while uniform regions of fast, tenuous wind emanate from higher latitudes. Fast and slow flow regimes are separated by a relatively sharp transition and the slow flow band, centered on the solar magnetic equator, is tilted relative to the heliographic equator. Typical tilts range from about 10° to 30°, reflecting observed tilts of the solar magnetic dipole relative to the rotation axis of the Sun. Gas dynamic and MHD simulations using this type of geometry provide a credible approximation to the gross latitudinal structure of the solar wind observed by Ulysses on the declining phase of the most recent solar activity cycle [e.g., *Phillips et al.*, 1995], and successfully reproduce the observed three-dimensional structure of CIRs over a wide range of latitudes out to distances of at least 5 AU [*Pizzo and Gosling*, 1994].

In the three-dimensional simulation used to produce Figure 9 [*Odstrcil and Pizzo*, 1999a], the slow flow band was 30° wide and was centered on the magnetic equator which, in turn, was tilted 20° relative to the heliographic equator. Initial conditions at the inner boundary at 0.14 AU were chosen to be 600 (300) km s^{-1}, 125 (500) cm^{-3} and 2 (0.5) x 10^6 K in the fast (slow) wind. These produced an ambient background state with speed 718 (359) km s^{-1}, density 2.08 (8,45) cm^{-3}, and temperature 1.30 (0.33) x 10^5 K in the fast (slow) wind at 1 AU, which are close to

typical observed values..

The CME was introduced at the inner boundary as a time-dependent pulse situated within the slow flow, centered at the point where the magnetic equator crosses the heliographic equator, with a cone half angle of 15° (see Figure 9). The pulse ramps were each 1 hour long and the pulse duration was 12 hours. Maximum values of radial velocity, density, and temperature within the pulse were 600 km s^{-1}, 1000 cm^{-3}, and 2 x 10^6 K, respectively. Thus, the radial velocity and temperature within the CME-like pulse were equal to the fast wind value and the pressure was 8 times greater than that in both the high and the low-speed ambient wind. Overall the initial pulse associated with the CME was shaped roughly like a prolate spheroid, with the long axis in the radial direction.

Figure 9 shows azimuthal slices of the resulting solar wind disturbance at four different polar angles 12 days after its launch from the inner boundary; Figure 10 shows a single meridional slice passing through the central longitude of the original perturbation obtained 10 days after launch. Originally confined to a 15° cone half angle, the CME has broadened by more than 30° in each transverse dimension. This spreading is a consequence of the high initial pressure within the CME as well as the additional pressure enhancement produced as the fast CME overtakes slower wind. The combined effects of radial flow collision, lateral material expansion, and interaction with a highly structured background solar wind velocity and density structure produce the bent and twisted pancake-like CME structure shown in Figures 9 and 10. The CME is retarded most near the equator where the CME plows directly into the slow, dense flow. In contrast, the high-latitude extensions of the CME are rapidly pulled outward by the fast flow there. Such effects are responsible for producing both the bowed-out appearance of the CME in Figure 10 as well as the systematic shift with latitude of the orientation of the CME in Figure 9. The CME is most compressed (thinnest) just north of the equator where it is swept into the CIR; the CME is most extended in the south where it is relatively free to expand in the high-speed flow there.

Beyond several AU, the steady state solution into which this CME was propagated contained corotating shocks aligned roughly along the nominal Archimedean spiral direction in the azimuthal direction but tilted in the meridional plane. At the central longitude of the CME, those shocks do not extend far below the equator (see, for example, Figures 1 and 2 in *Pizzo and Gosling* [1994]). The overall shock structure is significantly modified by the CME-driven disturbance. The shocks

can be discerned in Figures 9 and 10 as regions where the density contours are most closely spaced. Shock strengths are greatest, and the entire structure narrowest, where the forward and reverse shocks, driven by the relative motion and expansion of the CME, merge with the CIR shocks into a single shock pair north of the equator. At those latitudes the CME becomes entrained within the CIR. At southern latitudes a relatively weak forward shock - the result of both relative motion between the CME and the ambient wind and the expansion of the CME - stands well off in front of the CME. At the highest southern latitudes of the CME the front does not appear to be a shock. A relatively weak reverse shock, the result of overexpansion of the CME, trails most of the southern portion of the CME.

This three-dimensional simulation, although highly idealized, graphically demonstrates the complexities that arise in a CME-driven disturbance propagating into a spatially structured solar wind (see also *Odstrcil and Pizzo* [1999b]). The CME becomes distorted in all dimensions and the shock strengths and stand-off distances (relative to the CME) are strong functions of position. Even when the CME itself is spatially uniform close to the Sun, the disturbance the CME produces in the solar wind is a strong function of latitude and longitude as well as heliocentric distance.

Concluding Comments

Our goal in this paper has been to provide a simple physical description of fluid aspects of the evolution of CME-driven disturbances in the solar wind. This evolution becomes ever more complex as one proceeds from idealized speed perturbations introduced into a structureless solar wind using a simple one-dimensional fluid code to compound pressure and speed perturbations introduced into a solar wind that is highly structured in all three dimensions using a three-dimensional fluid code. Although the two and three-dimensional simulations provide unique global perspectives of disturbance evolution and include effects that simply can not be explored with the one-dimensional simulations, most of the basic physical processes and effects in both types of simulations are most simply understood in the context of the one-dimensional simulations.

We note that even the three-dimensional simulations are highly idealized approximations to what nature actually provides. The ambient solar wind nearly always contains detailed structure beyond

what is predicted by the tilted slow-wind band model. Not only is the flow usually spatially and temporally variable within both the slow-wind band and the high-speed wind, but also the slow-wind band almost always is warped rather than planar. The structure of the ambient solar wind can also be significantly modified by previous CME-driven disturbances, an effect that is more common near solar activity maximum than near solar activity minimum. In addition, it is unlikely that real CMEs provide initial perturbations that are as simple and spatially uniform as has been assumed in the simulations to date.

The inner boundary for all of the simulations discussed here lies well outside the critical point where the solar wind flow becomes supersonic. This choice simplifies the model calculations at the price that we learn little about how CMEs are initiated or evolve during the first 1/7th of their journey out to 1 AU. It also ensures that pressure perturbations produced in the wind do not propagate back to the inner boundary, since all pressure perturbations are superimposed on a highly supersonic outflow. Thus, for example, the reverse compression waves associated with over-expanding CMEs are convected outward with the rest of the wind, which would not be the case were the simulations initiated inside the critical point. We have suggested previously [*Gosling et al.* 1994b] that the reverse waves associated with overexpansion may actually be present in the solar wind only in CMEs that have supersonic speeds close to the solar surface. Such a class of supersonic CME events is clearly present in coronagraph observations [e.g., *Sheeley*, 1999]. For CMEs that have subsonic speeds close to the Sun, the reverse waves associated with overexpansion should propagate down to the lower atmosphere. We have previously suggested [*Gosling*, 1994] that, as it interacts with the lower atmosphere, such a reverse wave might produce a chromospheric effect known as a Moreton wave or, equivalently, a bright expanding ring in the lower corona [e.g., *Thompson et al.*, 1998].

Finally, for simplicity we have explicitly ignored effects of the magnetic field in all of our discussion despite the fact that CMEs are inherently a magnetic phenomenon. Moreover, it is the magnetic field that makes the solar wind behave like a fluid on all but the smallest scales [e.g., *Parker*, 1999]. It is expected, however, that the magnetic field plays a relatively minor role in solar wind dynamics because the momentum and energy density associated with the magnetic field usually are far less than that associated with the bulk flow of the plasma. And, as we have noted, in most CME-driven disturbances relative motion is the primary factor governing disturbance

evolution in the solar wind. Nevertheless, (1) the magnetic field increases the characteristic speed with which small amplitude pressure signals propagate in the wind, and (2) the magnetic pressure typically is comparable to, and can be greater than, the thermal pressure of the plasma, depending on the plasma beta (the ratio of plasma to magnetic field pressure). This indicates, for example, that solar wind disturbances spread more rapidly than is suggested by the fluid simulations, and overexpanding CMEs may actually be a result more of an enhanced magnetic pressure than an enhanced thermal pressure. We would not expect that either of these effects would seriously modify the conclusions drawn from the fluid simulations, although they would affect detailed comparisons of simulation results with observations.

In closing, we wish to emphasize that, even though the magnetic field usually plays a secondary role in disturbance evolution, it is a vital part of any CME-driven disturbance. Field line topology provides important clues for understanding CME origins in processes close to the Sun, and the strength and orientation of the field are crucial elements of a disturbance's interaction with the Earth's magnetosphere. Both the strength and orientation of the field are strongly affected by the evolution of CME-driven disturbances. The ambient field must drape about a fast CME as the CME pushes its way outward into the heliosphere, and the both the ambient field and that within the CME are enhanced as the plasma is compressed. Thus, a model that includes both fluid and magnetic field effects ultimately is needed for predicting space weather effects of these disturbances.

Acknowledgment. This paper is based on a tutorial presented at the SHINE workshop held in Boulder, Colorado in June, 1999. JTG thanks N. Crooker for travel support to the workshop. We thank D. Odstrcil and V. Pizzo for providing Figures 9 and 10 and J. Steinberg for comments on the manuscript. Work at Los Alamos was performed under the auspices of the U. S. Department of Energy with support from the National Aeronautics and Space Administration. Work at SAIC was performed with support from the National Aeronautics and Space Administration (Grant NASW-98007, SR&T program, and SEC-TP) and the National Science Foundation (Space Weather Program).

References

Crooker, N., J. A. Joselyn, and J. Feynman, editors, *Coronal Mass Ejections, Geophys. Monogr. Ser.*, vol. 99, pp 1-299, 1997.

Dryer, M. Interplanetary studies: Propagation of disturbances between the Sun and the magnetosphere, *Space Sci. Rev., 67*, 363, 1994.

Gosling, J. T., Coronal mass ejections in the solar wind at high solar latitudes: An overview, in *Proceedings of the Third SOHO Workshop: Solar Dynamic Phenomena and Solar Wind Consequences*, ESA SP-373, The Netherlands, pp 275-284, 1994.

Gosling, J. T., Coronal mass ejections, in *26th International Cosmic Ray Conference Invited, Rapporteur and Highlight Papers*, edited by B. Dingus, D. Kieda, and M. Salamon, AIP Conf. Proc., in press, 1999.

Gosling, J. T., and P. Riley, The acceleration of slow coronal mass ejections in the high-speed solar wind, *Geophys. Res. Lett., 21*, 2867, 1996.

Gosling, J. T., V. Pizzo, and S. J. Bame, Anomalously low proton temperatures in the solar wind following interplanetary shock waves: Evidence for magnetic bottles?, *J. Geophys. Res., 78*, 2001, 1973.

Gosling, J. T., E. Hildner, R. M. MacQueen, R. H. Munro, A. I. Poland, and C. L. Ross, The speeds of coronal mass ejection events, *Solar Phys., 48*, 389, 1976.

Gosling, J. T., D. N. Baker, S. J. Bame, W. C. Feldman, R. D. Zwickl, and E. J. Smith, Bidirectional solar wind electron heat flux events, *J. Geophys. Res., 92*, 8519, 1987.

Gosling, J. T., S. J. Bame, E. J. Smith, and M. E. Burton, Forward-reverse shock pairs

associated with transient disturbances in the solar wind at 1 AU, *J. Geophys. Res.*, *93*, 8741, 1988.

Gosling, J. T., S. J. Bame, D. J. McComas, J. L. Phillips, E. E. Scime, V. J. Pizzo, B. E. Goldstein, and A. Balogh, A forward-reverse shock pair in the solar wind driven by over expansion of a coronal mass ejection: Ulysses observations, *Geophys. Res. Lett.*, *21*, 237, 1994a.

Gosling, J. T., D. J. McComas, J. L. Phillips, L. A. Weiss, V. J. Pizzo, B. E. Goldstein, and R. J. Forsyth, A new class of forward-reverse shock pairs in the solar wind, *Geophys. Res. Lett.*, *21*, 2271, 1994b.

Gosling, J. T., D. J. McComas, J. L. Phillips, V. J. Pizzo, B. E. Goldstein, R. J. Forsyth, and R. P. Lepping, A CME-driven solar wind disturbance observed at both low and high heliographic latitudes, *Geophys. Res. Lett.*, *22*, 1753, 1995.

Gosling, J. T., P. Riley, D. J. McComas, and V. J. Pizzo, Overexpanding coronal mass ejections at high heliographic latitudes: Observations and simulations, *J. Geophys. Res.*, *103*, 1941, 1998.

Hundhausen, A. J., Some macroscopic properties of shock waves in the heliosphere, in *Collisionless Shocks in the Heliosphere: A Tutorial Review, Geophys. Monogr. Ser.*, vol. 34, edited by R. G. Stone and B. T. Tsurutani, pp 37-58, 1985.

Hundhausen, A. J., Coronal mass ejections, in *Cosmic Winds and the Heliosphere*, edited by J. R. Jokipii, C. P. Sonett, and M. S. Giampapa, University of Arizona Press, Tucson pp 259-296, 1997.

Hundhausen, A. J., and R. A. Gentry, Numerical simulation of flare-generated disturbances in the solar wind, *J. Geophys. Res.*, *74*, 2908, 1969.

Hundhausen, A. J., J. T. Burkepile, and O. C. St. Cyr, The speeds of coronal mass ejections: SMM observations from 1980 and 1984-1989, *J. Geophys. Res.*, *99*, 6543, 1994.

Montgomery, M. D., J. R. Asbridge, S. J. Bame, and W. C. Feldman, Solar wind electron temperature depressions following some interplanetary shock waves: Evidence for magnetic merging?, *J. Geophys. Res.*, *79*, 3103, 1974.

Odstrcil, D., M. Dryer, and Z. Smith, Propagation of an interplanetary shock along the heliospheric plasma sheet, *J. Geophys. Res.*, *101*, 19,973, 1996.

Odstrcil, D., and V. J. Pizzo, Three-dimensional propagation of coronal mass ejections (CMEs) in a structured solar wind flow 1. CME launched within the streamer belt, *J. Geophys. Res.*, *104*, 483, 1999a.

Odstrcil, D., and V. J. Pizzo, Three-dimensional propagation of coronal mass ejections (CMEs) in a structured solar wind flow 2. CME launched adjacent to the streamer belt, *J. Geophys. Res.*, *104*, 493, 1999b.

Parker, E. N., Sudden expansion of the corona following a large solar flare and the attendant magnetic field and cosmic ray effects, *Astrophys. J.*, *133*, 1014, 1961.

Parker, E. N., *Interplanetary Dynamical Processes*, Wiley Interscience, New York, 1963.

Parker, E. N., Space physics before the space age, in *Solar Wind Nine*, edited by S. R. Habbal, R. Esser, J. V. Hollweg, and P. A. Isenberg, AIP Conf. Proc., 471, Woodbury, NY, pp 3-13, 1999.

Pizzo, V. J., Interplanetary shocks on the large scale: A retrospective on the last decade's theoretical efforts, in *Collisionless Shocks in the Heliosphere: Reviews of Current Research, Geophys. Monogr. Ser.*, vol. 35, edited by B. T. Tsurutani and R. G. Stone, pp 51-68, 1985.

Pizzo, V. J., The evolution of corotating stream fronts near the ecliptic plane in the inner solar system, 2. Three-dimensional tilted-dipole fronts, *J. Geophys. Res.*, *96*, 5405, 1991.

Pizzo, V. J., Global, quasi-steady dynamics of the distant solar wind, 1, Origins of north-south flows in the outer heliosphere, *J. Geophys. Res.*, *99*, 4173, 1994.

Pizzo, V. J., Global modeling of CME propagation in the solar wind, in *Coronal Mass Ejections, Geophys. Monogr. Ser.*, vol. 99, edited by N. Crooker, J. A. Joselyn, and J. Feynman, pp 261-267, 1997.

Pizzo, V. J., and J. T. Gosling, 3-D simulation of high-latitude interaction regions: Comparison with Ulysses results, *Geophys. Res. Lett.*, *21*, 2063, 1994.

Phillips, J. L., S. J. Bame, W. C. Feldman, B. E. Goldstein, J. T. Gosling, C. M. Hammond, D. J. McComas, M. Neugebauer, E. E. Scime, and S. T. Suess, Ulysses solar wind plasma observations at high southerly latitudes, *Science*, *268*, 1030, 1995.

Richardson, I. G., and H. V. Cane, Regions of abnormally low proton temperature in the solar wind (1965-1991) and their association with ejecta, *J. Geophys. Res.*, *100*, 23,397, 1995.

Riley, P., CME dynamics in a structured solar wind, in *Solar Wind Nine*, edited by S. R. Habbal, R. Esser, J. V. Hollweg, and P. A. Isenberg, AIP Conf. Proc., 471, Woodbury, NY, pp 131-136, 1999.

Riley, P., and J. T. Gosling, Do coronal mass ejections implode?, *Geophys. Res. Lett.*, *25*, 1529, 1998.

Riley, P., J. T. Gosling, and V. J. Pizzo, A two-dimensional simulation of the radial and latitudinal evolution of a solar wind disturbance driven by a fast, high-pressure coronal mass

ejection, *J. Geophys. Res., 102*, 14,677, 1997.

Sheeley, N. R., Using LASCO observations to infer solar wind speed near the Sun, in *Solar Wind Nine*, edited by S. R. Habbal, R. Esser, J. V. Hollweg, and P. A. Isenberg, AIP Conf. Proc., 471, Woodbury, NY, pp 41-45, 1999.

Sheeley, N. R., J. H. Walters, Y.-M. Wang, and R. A. Howard, Continuous tracking of coronal outflows, *J. Geophys. Res., 104*, 24,739, 1999.

Simon, M., and W. I. Axford, Shock waves in the interplanetary medium, *Planet. Space Sci., 14*, 901, 1966.

Thompson, B. J., S. P. Plunkett, J. B. Gurman, J. S. Newmark, O. D. St. Cyr, and D. J. Michels, SOHO/EIT observations of an Earth-directed coronal mass ejection on May 12, 1997, *Geophys. Lett., 25*, 2465, 1998.

Figure Captions

Figure 1. Simulated solar wind speed and pressure versus heliocentric distance 83 and 250 hours after introducing a 300 km s^{-1} step function increase in speed at 0.14 AU. Vertical lines bound the last 30 hours of slow wind introduced into the simulation prior to the speed increase. Adapted from *Gosling and Riley* [1996].

Figure 2. Simulated solar wind speed and pressure versus heliocentric distance 83 and 250 hours after introducing a 300 km s^{-1} step function decrease in speed at 0.14 AU. Vertical lines bound the first 30 hours of slow wind introduced at the inner boundary. Adapted from *Gosling and Riley* [1996].

Figure 3. Simulated solar wind speed and pressure versus heliocentric distance for a solar wind disturbance initiated by a 15-hour long, 250 km s^{-1}, square wave increase in speed at 0.14 AU. The snapshots shown were obtained 27, 69 and 125 hours after onset of the perturbation. Vertical lines bound the material introduced at higher speed at the inner boundary, and thus mark the CME in the simulation. Adapted from *Gosling* [1999].

Figure 4. Simulated solar wind speed and pressure versus heliocentric distance for a solar wind disturbance initiated by a 15-hour long, 150 km s^{-1}, square wave decrease in speed at 0.14 AU. The snapshots shown were obtained 41 and 111 hours after onset of the perturbation. Vertical lines bound the material introduced at lower speed at the inner boundary, and thus mark the CME in the simulation. Adapted from *Gosling* [1999].

Figure 5. Simulated solar wind speed and pressure versus heliocentric distance for a solar wind disturbance initiated by a 10-hour long, factor of four, bell-shaped increase in density at 0.14 AU. The snapshots shown were obtained 55 and 194 hours after onset of the perturbation. Vertical lines bound the material within the density pulse, and thus identify the CME in the simulation. Adapted from *Gosling et al.* [1998].

Figure 6. Solar wind speed and pressure versus heliocentric distance for three simulated disturbances, obtained 59.1 hours after initiation at 0.14 AU. In the left, center, and right panels respectively the disturbances were initiated by increasing the density by a factor of four, by increasing the speed by a factor of two, and by increasing both the density (by a factor of four) and the speed (by a factor of two) in bell-shaped pulses 10-hours long. Vertical lines bracket the plasma originally within the bell-shaped pulses at the inner boundary and thus identify the CMEs in the simulation. Adapted from *Gosling et al.* [1995].

Figure 7. Solar wind speed and pressure versus heliocentric distance for two simulated disturbances, obtained 83 and 250 hours after initiation at 0.14 AU. In the left and right panels respectively, the disturbances were initiated by decreasing the speed by 300 km s^{-1} and by simultaneously decreasing the speed by 300 km s^{-1} and increasing the density by a factor of four in bell-shaped pulses 30-hours long. Vertical lines bracket the plasma originally within the bell-shaped pulses at the inner boundary and thus identify the CMEs in the simulations. Adapted from *Gosling and Riley* [1996].

Figure 8. Upper panels: Color-coded, meridional plots of simulated radial velocity, meridional velocity, and pressure 6.9 days after the initiation of the disturbance at 0.14 AU. The disturbance was initiated in this two-dimensional simulation as a 10-hour long, bell-shaped pulse with a speed equal to that of the ambient, high-latitude wind and a maximum pressure 6 times greater than that in the ambient solar wind at both high and low latitudes. At the inner boundary the pulse extended from the equator up to a latitude of 45°. The solid line in each panel marks the boundary of the material originally within the bell-shaped pulse and thus identifies the CME in the simulation. Lower panels: Same as in the upper panels except that the difference between the solution at 6.9 days and the steady state solution is shown. Adapted from *Riley et al.* [1997].

Figure 9. Left: Schematic illustrating the geometry of the three-dimensional simulation at 0.14 AU. A 30° band of slow, dense wind, tilted at 20° to the heliographic equator encircles the Sun. It is surrounded on either side by fast, tenuous wind extending up to the polar regions of the Sun. The initial perturbation filled a 15° cone centered in the low-speed wind at the heliographic

equator. Plasma within the pulse, which lasted for 14 hours, had the same speed as the high-latitude wind and an internal pressure eight times greater than that within the ambient wind at both high and low latitudes. Right: Longitudinal slices of the disturbance at four different polar angles 12 days after its launch from 0.14 AU. The slices extend from 2.5 to 5 AU and cover azimuths from 50° to 130°. The initial disturbance was centered at an azimuth of 90°. The radial velocity is indicated by the gray scale and the density is indicated by contours. The injected material density, representing the CME, is normalized to 1 AU values and is color-coded. Adapted from *Odstrcil and Pizzo* [1999a].

Figure 10. Similar to Figure 9 except that this shows a meridional cut at the central longitude of the disturbance obtained 10 days after the initial perturbation at 0.14 AU. The cut extends from 1 to 5 AU and covers polar angles from 30° to 150°. Adapted from *Odstrcil and Pizzo* [1999b].

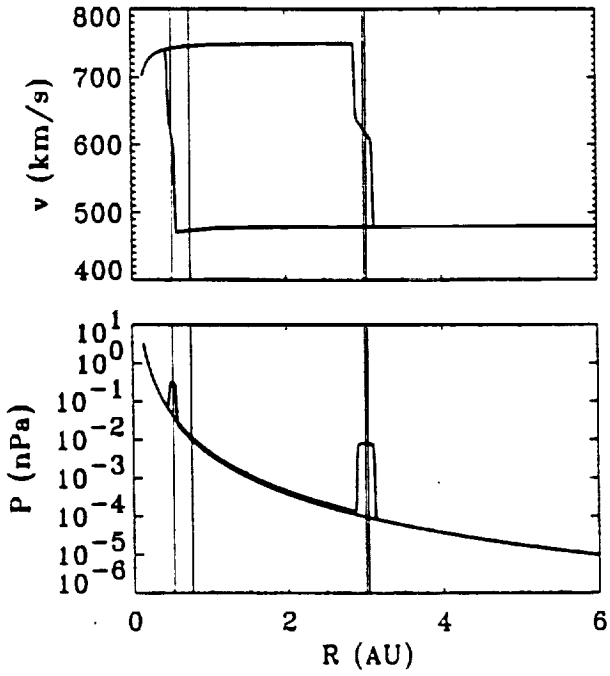
800
700
600
500
400
v (km/s)
10^{1}
10^{0}
10^{-1}
10^{-2}
10^{-3}
10^{-4}
10^{-5}
10^{-6}
P (nPa)
0
2
4
6
R (AU)

Figure 1

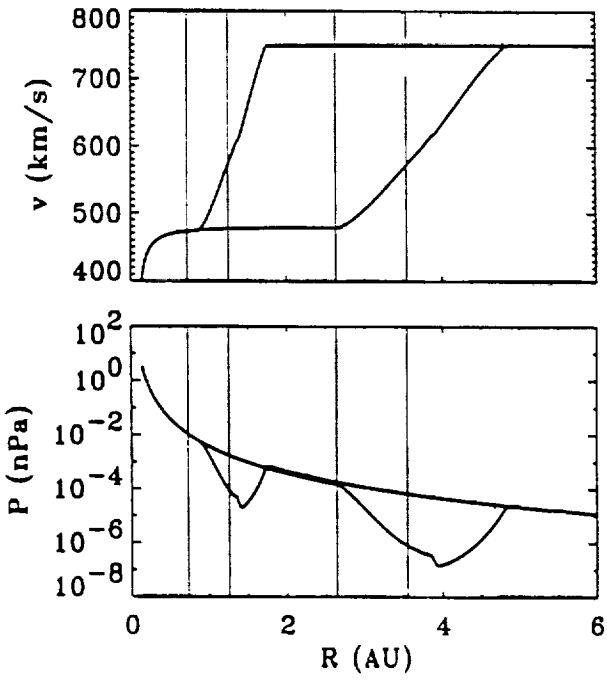

Figure 2

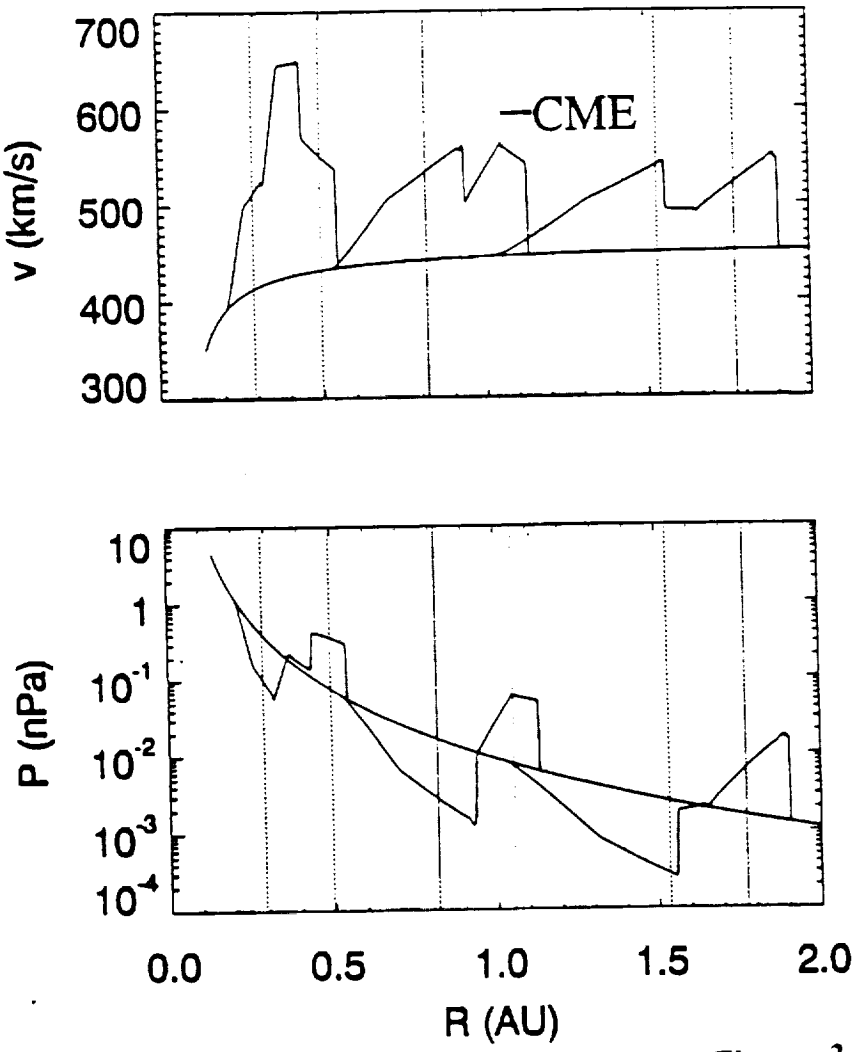
700
600
500
400
300
v (km/s)
CME
10
1
10^{-1}
10^{-2}
10^{-3}
10^{-4}
P (nPa)
0.0
0.5
1.0
1.5
2.0
R (AU)

Figure 3

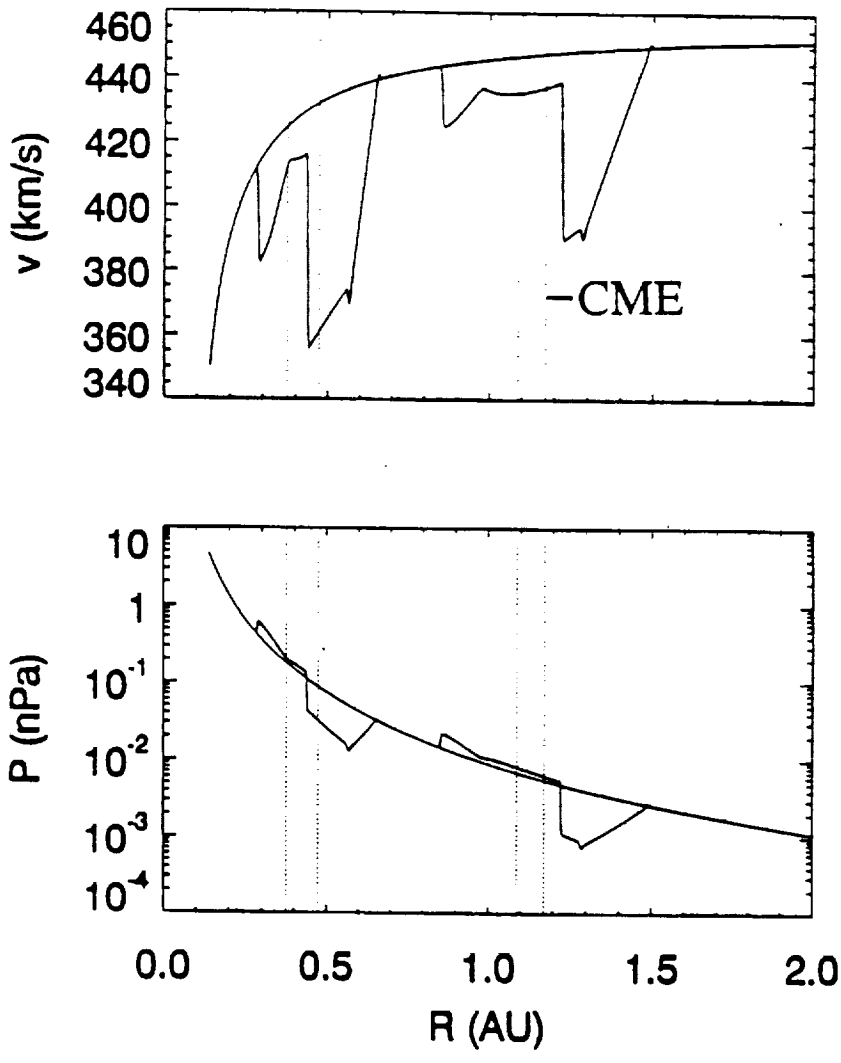
460
440
420
400
380
360
340
v (km/s)
CME
10
1
10^-1
10^-2
10^-3
10^-4
P (nPa)
0.0
0.5
1.0
1.5
2.0
R (AU)

Figure 4

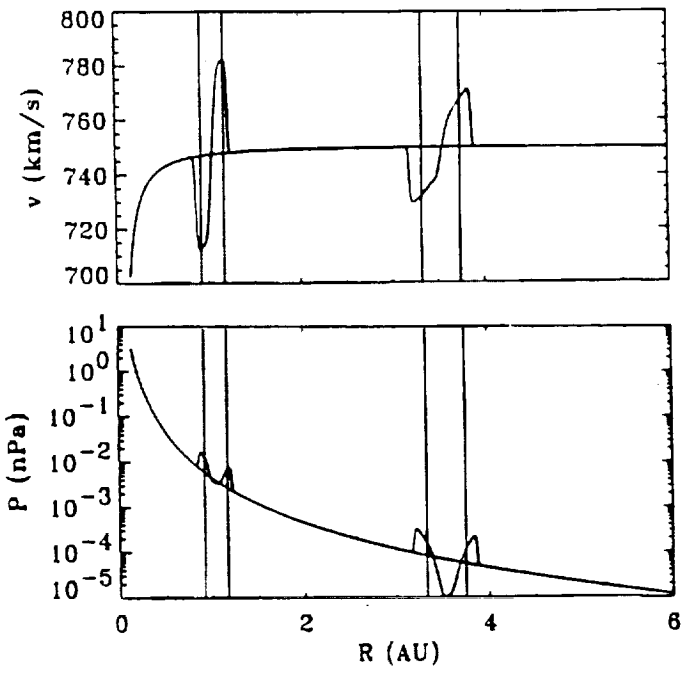
800
780
760
740
720
700
v (km/s)
10^1
10^0
10^{-1}
10^{-2}
10^{-3}
10^{-4}
10^{-5}
P (nPa)
0
2
4
6
R (AU)

Figure 5

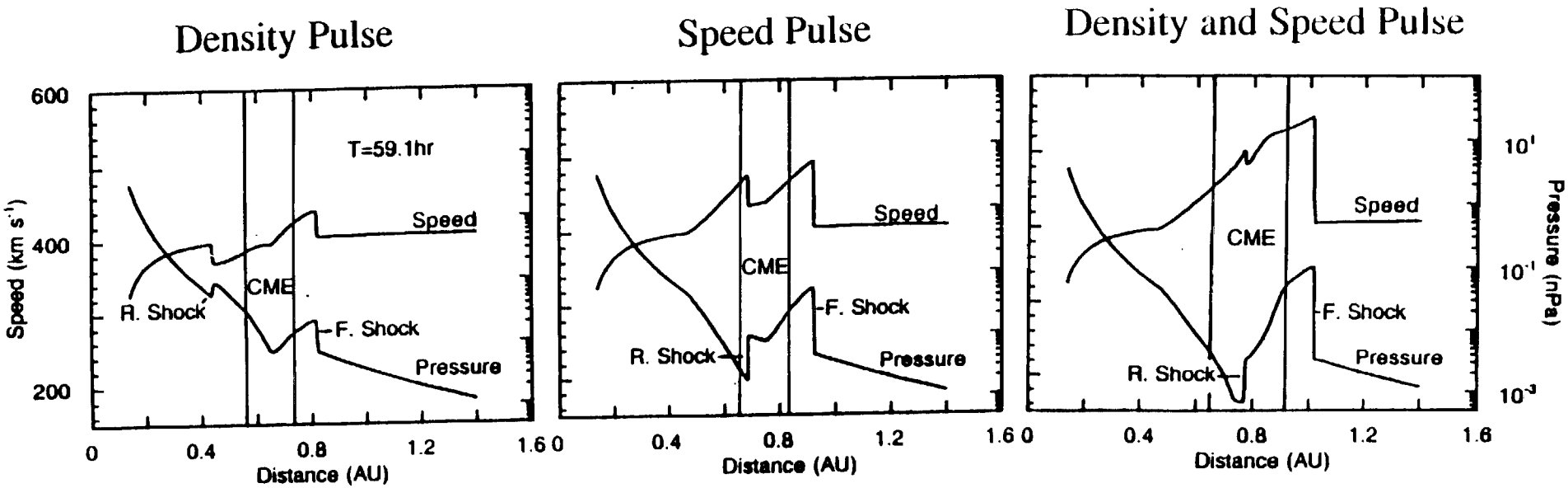
Density Pulse
Speed Pulse
Density and Speed Pulse
600
400
200
Speed (km s⁻¹)
T=59.1hr
Speed
CME
R. Shock
F. Shock
Pressure
0
0.4
0.8
1.2
1.6
Distance (AU)
10¹
10⁻¹
10⁻³
Pressure (nPa)

Figure 6

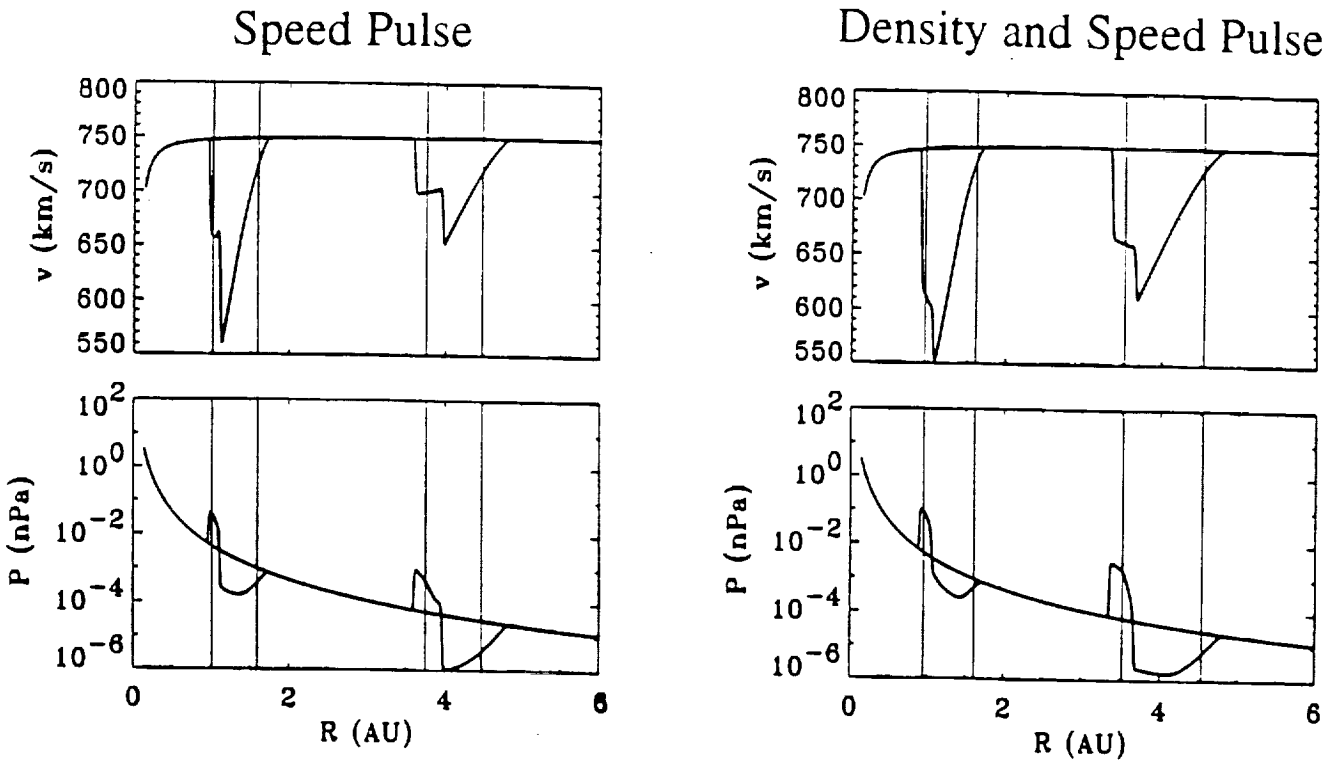
Speed Pulse
Density and Speed Pulse
v (km/s)
800
750
700
650
600
550
P (nPa)
10^2
10^0
10^{-2}
10^{-4}
10^{-6}
0
2
4
6
R (AU)

Figure 7

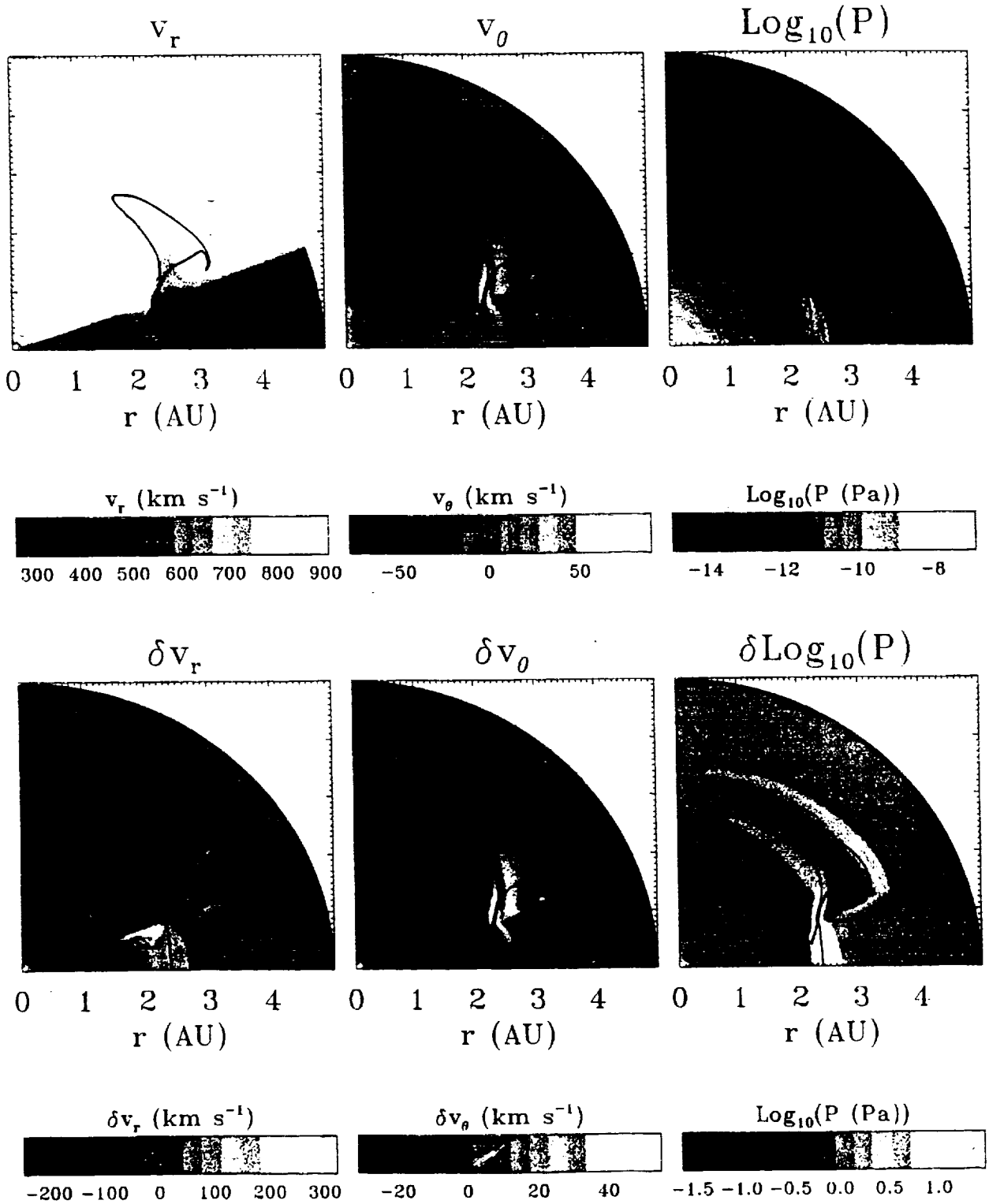
v_r
v_θ
$Log_{10}(P)$
0 1 2 3 4
r (AU)
v_r (km s^{-1})
300 400 500 600 700 800 900
v_θ (km s^{-1})
−50 0 50
Log_{10}(P (Pa))
−14 −12 −10 −8
δv_r
δv_θ
$\delta Log_{10}(P)$
δv_r (km s^{-1})
−200 −100 0 100 200 300
δv_θ (km s^{-1})
−20 0 20 40
Log_{10}(P (Pa))
−1.5 −1.0 −0.5 0.0 0.5 1.0

Figure 8

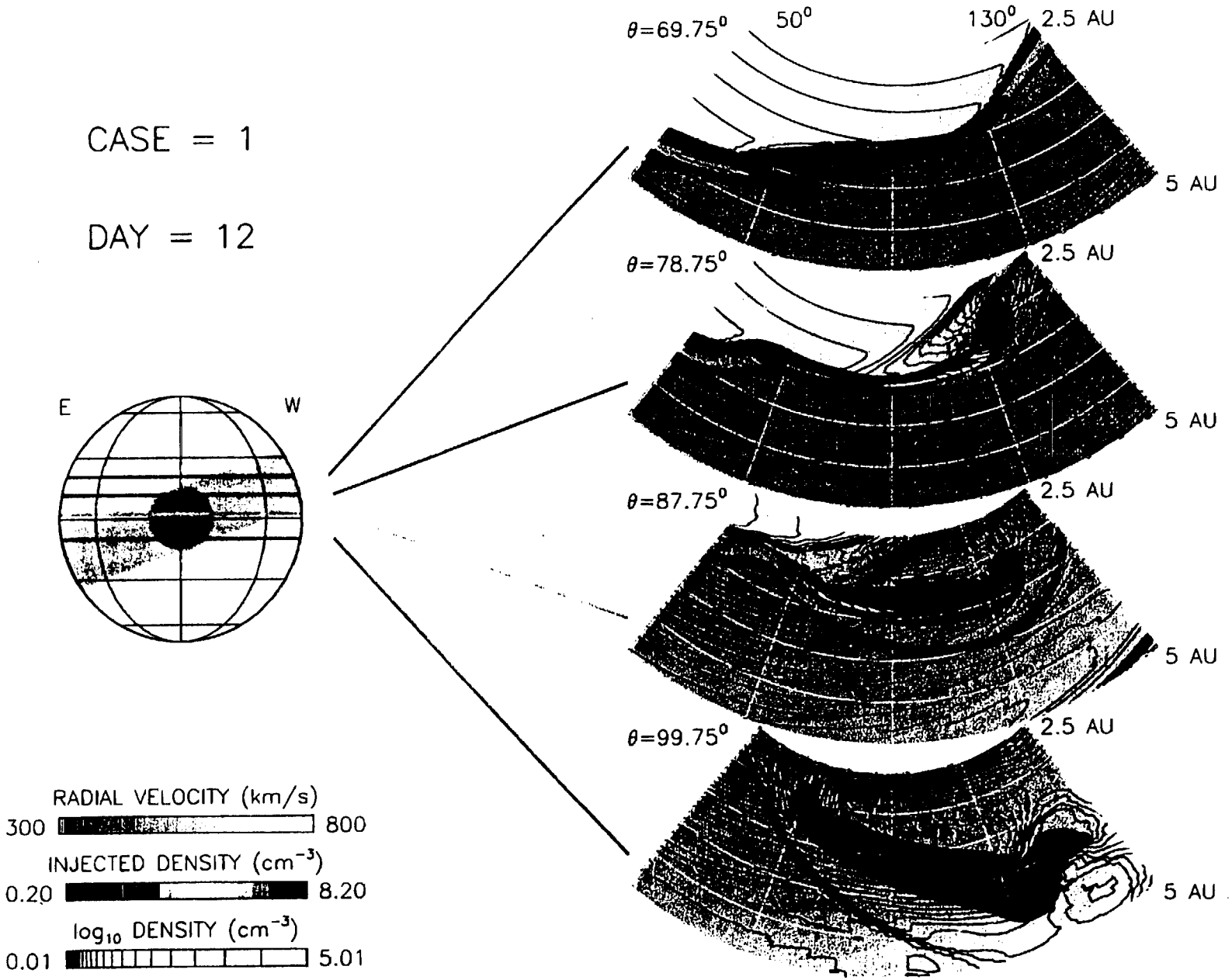
CASE = 1
DAY = 12
E
W
θ=69.75°
50°
130°
2.5 AU
5 AU
θ=78.75°
2.5 AU
5 AU
θ=87.75°
2.5 AU
5 AU
θ=99.75°
2.5 AU
5 AU
RADIAL VELOCITY (km/s)
300
800
INJECTED DENSITY (cm⁻³)
0.20
8.20
log10 DENSITY (cm⁻³)
0.01
5.01

Figure 9

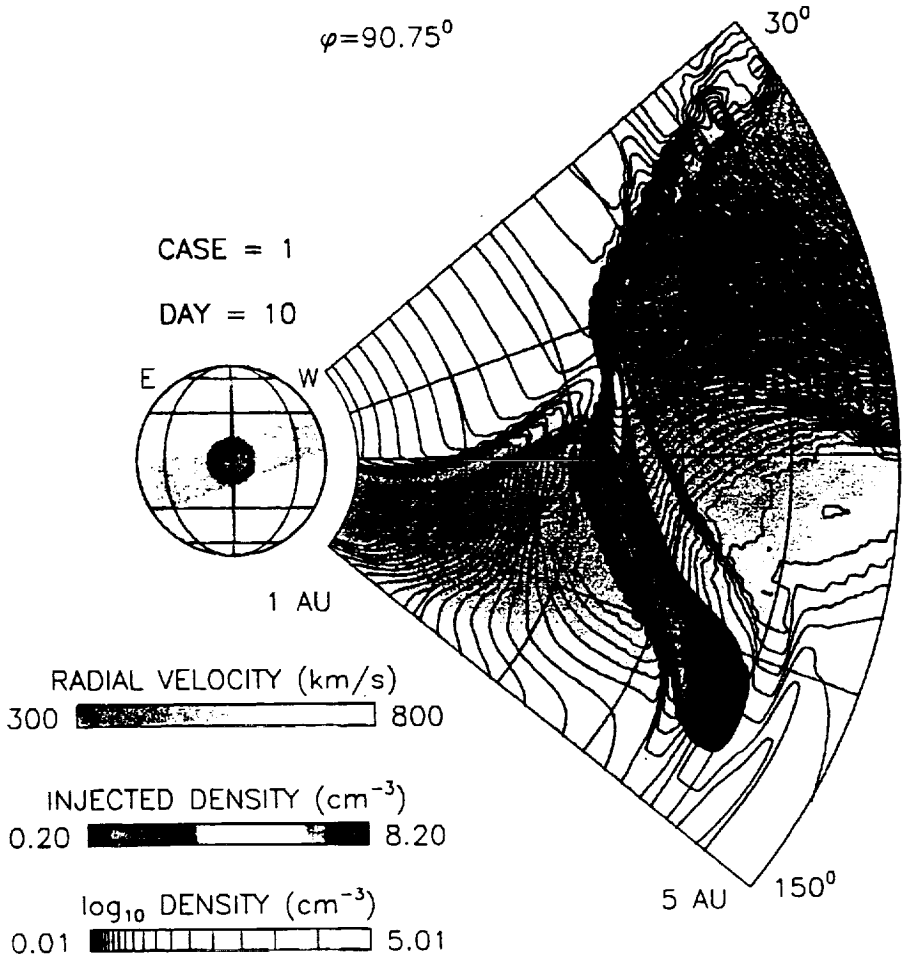
φ=90.75°
30°
CASE = 1
DAY = 10
E
W
1 AU
5 AU
150°
RADIAL VELOCITY (km/s)
300
800
INJECTED DENSITY (cm⁻³)
0.20
8.20
log₁₀ DENSITY (cm⁻³)
0.01
5.01

Figure 10

Appendix 3

On the polytropic relationship between density and temperature within CMEs: Numerical simulations

Pete Riley, J. T. Gosling, and V. J. Pizzo

To be Submitted to the *Journal of Geophysical Research*, February, 2000.

On the Polytropic Relationship between Density and Temperature within CMEs: Numerical Simulations

Pete Riley

Science Applications International Corporation, San Diego, California.

J. T. Gosling

Los Alamos National Laboratory, Los Alamos, New Mexico.

V. J. Pizzo

Space Environment Center, NOAA, Boulder, Colorado.

Abstract. There is currently debate concerning the interpretation of the negative correlation that is often observed between electron density and electron temperature within CMEs at a fixed point in space. If on one hand, these single spacecraft observations provide direct measures of the polytropic properties of the plasma, then they imply that the polytropic index for the electrons, γ_e is often less than 1. Moreover, since the electrons carry the bulk of the pressure (via their significantly higher temperature) this further implies that the dynamics of CME evolution are dominated by an effective polytropic index, $\gamma_{eff} < 1$. On the other hand, $\gamma < 1$ implies that as the ejecta propagate away from the Sun and expand, they also heat up; a result clearly at odds with in situ observations. In contrast, many studies have shown that the quiescent solar wind exhibits a positive correlation between electron density and temperature, suggesting that $\gamma_e > 1$. In this study, we utilize a one–dimensional, single–fluid model mimicking the evolution of CMEs and their associated disturbances in the solar wind to address the correct interpretation of the relationship between electron density and temperature within CMEs at fixed points in space. Although we impose a polytropic relationship (with γ = constant) throughout our simulations, we demonstrate that, at fixed locations, a variety of types of correlation between density and temperature can be observed. Furthermore, we show that the presence of uncorrelated fine–scale structure is all that is required to produce the types of negative correlation that are often seen within CMEs. Consequently, we conclude that a negative correlation between electron density and temperature, observed at a single point in space, cannot be used to infer the value of γ_e Instead, we suggest that fine–scale fluctuations in pressure together with the plasma tendency to achieve pressure balance with its surroundings are responsible for the observed profiles.

1. Introduction

A number of studies have demonstrated that a negative correlation often exists between electron density (n_e) and temperature (T_e) within magnetic clouds [e.g., *Osherovich et al.*, 1993a,b], and more generally, coronal mass ejections (CMEs) [e.g., *Hammond et al.*, 1996]. In particular, *Osherovich et al.* [1993a] found that, on average, the slope of logarithmic plot of T_e versus n_e equaled \1/2 within magnetic clouds. These results are in contrast to studies of the quiescent solar wind at different heliocentric distances for which a positive correlation is found [e.g., *Sittler and Scudder,* 1980; *Pilipp et al.*, 1990; *Phillips et al.*, 1993; *Phillips et al.*, 1995].

The relationship between temperature and density in a plasma has important ramifications for hydrodynamic and MHD models of space plasmas, and particularly models of CME evolution in the solar wind, since most models do not explicitly include energy conservation in their description of the fluid [e.g., *Riley,* 1999]. Instead, they close the system of equations by assuming that the entropy of a fluid element remains constant as the system evolves. Thus the energy transport equation is simply,

$$\frac{\partial}{\partial t}\left(\frac{P}{n^{\gamma}}\right)+v\cdot\nabla\left(\frac{P}{n^{\gamma}}\right)=0 \qquad (1)$$

where P is the thermal pressure, n is the number density, γ is the polytropic index, and v is the bulk velocity of the plasma. Combining this with the equation for an ideal gas, $P = nK_BT$, leads to:

$$\frac{D}{Dt}\left(\frac{T}{n^{\gamma-1}}\right)=0 \qquad (2)$$

where K_B is the Boltzmann constant, T is the temperature of the plasma, and we have replaced the temporal (Eulerian) and spatial derivatives with the total (Lagrangian) derivative (D/Dt). Thus along any streamline,

$$Log(T) = (\gamma - 1)Log(n) + Log(S) \tag{3}$$

where the constant, S, is the thermodynamic entropy of the plasma. If equation (3) holds then the slope of a logarithmic plot of T versus n should yield a straight line with with a slope equal to (γ–1) and an intercept related to the entropy of the plasma.

Osherovich and colleagues [e.g., *Osherovich et al.*, 1993a,b, 1995 *Fainberg et al.*, 1996; *Osherovich et al.*, 1998, 1999] argued that equation (3) holds for single–point spacecraft measurements of magnetic clouds in the interplanetary medium. Although strictly the relationship holds only along a given streamline, they contend that because of the assumed axisymmetry of their model, together with the assumption of infinite conductivity, the entropy term must be constant throughout the magnetic cloud. Furthermore, they reason that the entropy term cannot vary significantly during the passage of the magnetic cloud, for otherwise there would not be a unique linear relationship between $Log(T)$ and $Log(n)$ as is commonly observed.

Osherovich et al. [1993a] derived an analytic theory for the evolution self–similar, axisymmetric, radially–expanding, magnetic flux ropes and applied the model to magnetic clouds in the solar wind., Their solution, however, required $\gamma < 1$ to produce the observed expansions of clouds. On the other hand, *Vandas et al.* [1996] modeled the evolution of force–free objects within an ambient solar wind flow using three–dimensional MHD simulations and showed that a good agreement could be found

between the simulation results and *Osherovich et al.'s* analytic theory without the requirement that $\gamma < 1$ in the simulations.

Osherovich and Burlaga [1997] analyzed several magnetic clouds, as well as the sheath region that surrounded them and the ambient solar wind. They found that the application of equation (3) to each region yielded electron polytropic indices of 0.4–0.5 (for the magnetic cloud), 0.7–0.8 (for the sheath region), and 1.2 (for the ambient solar wind). From this, they concluded that "single–fluid MHD models can approximate any one of these states, but not all three".

Other studies, however, have disputed the polytropic interpretation of the n_e– T_e relationship within magnetic clouds. *Hammond et al.* [1996] studied the relationship between core electron temperature and density and found a similar negative correlation for 5 CMEs that were observed by the Ulysses spacecraft during its in–ecliptic journey from Earth to Jupiter. They also found that a negative correlation existed during CME – but not cloud–like – intervals, when axisymmetry was probably not a good assumption. They suggested that the core n_e– T_e profile is not the result of a polytropic relationship, but derives from differences in the collision histories of the electrons, i.e., denser plasma cools more quickly than less dense plasma.

Gosling [1999] has also argued against the inference that the polytropic index is less than one and thus that single–point measurements cannot be used to infer the value of γ_e. He showed that if $\gamma_e < 1$, then the temperature within CMEs must increase as they propagate away from the Sun, a result that is clearly at odds with both solar observations and in situ CME observations at different heliocentric distances. He suggested that the observed relationship occurs primarily because of the plasma's tendency to reach local pressure balance.

Skoug et al. [1999] studied a single CME observed by both ACE and Ulysses at widely different heliocentric distances. They showed that while the slope derived from each spacecraft individually was indeed negative, the least squares fit for the combined ACE–Ulysses data set was positive and yielded $\gamma_e = 1.4$.

Using the relationship between density and temperature, derived from measurements at different heliocentric distances, to determine the polytropic relationship of electrons and protons in the general solar wind appears to be on firmer ground. *Gosling* [1999] has reviewed many of these studies. Here we only remark that most studies found parameters in the ranges $\gamma_p = 1.4 - 1.6$ and $\gamma_e = 1.1 - 1.6$. Suffice to say, that $\gamma > 1$ for both electrons and protons in the normal solar wind. *Newbury et al.* [1997] found a positive correlation between proton density and temperature in the vicinity of stream interfaces but cautioned that care must be taken to isolate solar wind from different coronal source regions. In particular, they presented an event for which a negative correlation was found between density and temperature when data both preceding and following a stream interface were plotted collectively. On the other hand, when the data were separated into two sets (an interval preceding the interface and an interval following it), each displayed a positive correlation. *Skoug et al.* [1999] also identified intervals within the ACE and Ulysses datasets that were not associated with CMEs yet also displayed a negative correlation.

In this study, we use numerical simulations to investigate the relationship between fluid density and temperature for a variety of perturbations, some of which have been shown previously to mimic the propagation and evolution of CMEs through the solar wind. We reduce the modeling to its simplest terms; we consider a single fluid, spherically symmetric system and neglect magnetic fields. We will demonstrate that, in spite of these simplifications, we can generate a a variety of relationships between n and T depending

on the launch profiles. Since our fluid algorithm strictly enforces γ = constant (3/2 – 5/3) throughout the simulation domain, we conclude that a departure in the slope from (γ–1) does not indicate a change in the polytropic index of the gas. We will also demonstrate that fine–scale random perturbations in density and temperature are all that are required to produce the types of negative n–T correlation that are often observed in magnetic clouds. Thus we conclude that single–point measurements of density and temperature may not be a good measure of γ.

2. Simulation Technique

To mimic the evolution of a CME–driven disturbance in the solar wind, we employ an Eulerian finite difference code [*Stone and Norman,* 1992]. The energy transport equation is reduced to equation (1) and the polytropic index, γ=constant. For the simulations presented here, we set γ=3/2, however, selected runs were also made with γ =5/3 with no substantial differences. The code has been previously applied to modeling CME disturbances in one and two dimensions [e.g., *Gosling and Riley,* 1996; *Riley et al.,* 1997; *Gosling et al.,* 1998; *Riley and Gosling,* 1998]. Since our goal is to investigate the relationship between n and T at fixed locations in space for a variety of perturbations, and not to reproduce the details of CME evolution in the solar wind, we make a number of simplifying assumptions. First, we neglect the magnetic field. Thus our simulations are strictly only valid for high–β CMEs. Second, we restrict our analysis to a spherically symmetric (one–dimensional) geometry. As such, the interactions between adjacent parcels of plasma are probably too strong, since velocity shear transverse to the radial direction is not permitted. A practical benefit of these assumptions is that the simulations are computationally fast. Thus we can explore the evolution of a variety of launch

profiles within a relatively short amount of time. Although only a handful of cases are summarized in this report, in total, >200 launch profiles were simulated and analyzed.

The simulations consist of two parts; first an ambient solar wind is built and then a perturbation is introduced at the inner boundary. To produce an ambient solar wind, we specify the speed, density and temperature at the inner boundary of the simulation (30 R_{Sun}). We enforce inflow boundary conditions at the inner boundary and outflow boundary conditions at the outer boundary (6 AU). The simulation region is filled with approximately correct values and allowed to reach an equilibrium flow. Values of n=128 cm^{-3}, v=702 km s^{-1}, and T=10^6 K at the inner boundary yielded the equilibrium flow profiles summarized in Figure 1 and match well with Ulysses observations at high heliographic latitudes. In the present study, the particular values of the ambient wind are largely immaterial; we could have chosen values more indicative of the slow solar wind. This would only have had the effect of increasing the time taken to complete a particular simulation without affecting our conclusions.

Introducing a time–dependent perturbation can, in principle, mimic the launch of a CME through the inner boundary of the simulation. We varied: (1) the shape of the pulse (square– and bell–shaped); (2) the duration of the pulse (10, 30, and 50 hours); (3) the height of the pulse (×4, ×10, and ×30 above or below ambient values; and (4) which parameters were perturbed (density, temperature, and or speed). In addition, in some perturbations, the speed was linearly increased or decreased. Some of these profiles have been previously shown to compare favorably with observed CME–driven disturbances in the solar wind [e.g., *Gosling and Riley,* 1996; *Riley et al.,* 1997; *Gosling et al.,* 1998]. Others are probably not related to any observed event. Nevertheless, they allow us to explore how different perturbations evolve as they propagate through the solar wind, and in particular, how density and temperature are related at fixed locations in space.

In addition to these large–scale perturbations, we also modeled fine–scale random perturbations in density and temperature. We added this noise both to the ambient solar wind flow and to the large–scale perturbation profiles.

3. Results

We have chosen seven examples from the set of simulations to support the main conclusion of this study, namely that in spite of the fact that γ=constant in the model, a variety of relationships between density and temperature can be observed at fixed heliocentric distances. Thus single–point spacecraft measurements of n and T cannot, in general, be used to infer γ. The first five examples consist of large–scale perturbations (summarized in Figure 2), while the last two examples consist of fine–scale random fluctuations in density and temperature.

The perturbation for our first case study is summarized in Figure 2a. It consists of a bell–shaped increase in speed of 300 km s^{-1} above the ambient speed in concert with a ×4 enhancement in both density and temperature. Thus the gas pressure peaks at ×16 above background values. The perturbation lasts for 50 hours. These variations approximate a fast, dense, hot CME propagating through a slower, more tenuous, and cooler ambient solar wind. Figure 3 shows the resulting solar wind disturbances at 55 and 194 hours following its launch. The two pairs of vertical lines in each panel mark the boundary of the pulse. The development and evolution of this type of disturbance is well known and discussed elsewhere [e.g., *Hundhausen and Gentry,* 1969; *Riley et al.,* 1997]. Our interest here lies in the variation of temperature and density at a fixed location in space, since this is how single–spacecraft measurements are made. In Figure 4 we plot temperature against

density logarithmically at 2.5 AU. The cross marks the ambient solar wind, which, at a particular location has a single value. The dots identify disturbed solar wind, and those dots with diamonds superimposed on them identify the ejecta. Inspection of Figure 3 reveals that the temporal sense of the curve: From the ambient solar wind (the cross), the sheath region of the disturbance (dots that move from the lower left to the top of the Figure then to the upper right) is sampled. Next, the ejecta (diamonds that migrate from the upper right to the lower left then curl under) is encountered and finally ambient solar wind flow is again sampled. The solid straight line is a least–squares fit to the ejecta portion and has a numerical value of 0.643. If this slope were indicative of the polytropic index of the gas, we would infer a value, γ=1.643. This is similar – but not identical – to the model value of 1.5.

The perturbation used for our second example is summarized in Figure 2b. Both the speed and temperature are held constant while the density (and hence pressure) is increased smoothly by a factor of 4 and then returned to its equilibrium value over a period of 30 hours. This type of pulse was used to successfully model a new class of CMEs observed at high heliographic latitudes by the Ulysses spacecraft [*Gosling et al.*, 1994]. Figure 5 summarizes the plasma density and temperature variations at 1.5 and 3.5 AU. The ejecta and sheath regions are now much more symmetric with respect to the temporal midpoint of the ejecta (where the temperature is a minimum). The least–squares fit to the results of Figure 5a lead to a slope of –0.725, whereas the fit to Figure 5b leads to a slope of 1.859. The sheath region in both panels (dots) maintains a slope of ~0.5.

For our third example, we consider a perturbation in speed only. The initial profile of the pulse is shown in Figure 2c. The speed is decreased by 300 km s^{-1} over an interval of 30 hours and then returned to its initial value while maintaining constant density and temperature. Since density and temperature do not change, thermodynamic entropy also

remains constant. *Gosling and Riley* [1996] have discussed this type of pulse in relation to the acceleration of CMEs in the high–speed solar wind. In Figure 6 we compare density and temperature at 1.5 and 3.5 AU from the Sun. The least–squares fit gives +0.600 and –0.378, respectively. The sheath region, at both locations, gives a slope of ~0.5. The straight–line portion of the sheath region extending from the ambient solar wind point (cross) to the lower left corner of each panel occurs in the region trailing the CME and corresponds to a rarefaction (see Figure 3 of *Gosling and Riley* [1996]). Figures 6a and 6b suggest that the sense of the inferred slope changes with heliocentric distance. Inspection of plots at other heliocentric distances (not shown) confirms that the ejecta profile evolves from a predominantly positive slope near the Sun to a predominantly negative slope at larger heliocentric distances.

The perturbation for our fourth example is shown in Figure 2d. This profile consists of smooth decrease in density (by a factor of 4) with a corresponding increase in temperature – so as to maintain constant pressure – over a period of 10 hours while maintaining constant speed. Figure 7 displays the relationship between temperature and density at 3.5 AU. The least–squares fit to the ejecta portion of the data gives a slope of –1.016. Again, the slope of the sheath region equals 1/2.

As our final example, we consider a perturbation in density and temperature, such that the entropy of gas remains constant. From equation (3) we have that the thermodynamic entropy, $S = T/n^{(\gamma-1)}$, which for γ=3/2 becomes $S = T/n^{1/2}$. Thus if the pulse consists of a peak density enhancement of ×4, then it must be accompanied by a corresponding peak temperature increase of ×2 to maintain constant entropy. Thus the peak pressure is ×6 above ambient values. The resulting relationship between density and temperature at 3.5 AU is shown in Figure 8. The least squares fit to the ejecta gives a slope of 0.490. Note that although this perturbation is qualitatively similar to our second example (compare

Figures 2b and 2e), the resulting temperature–density relationship is significantly different (compare Figures 5 and 8).

4. Summary and Discussion

In this report we have shown that one–dimensional, hydrodynamic simulations of the evolution of CME–driven disturbances in the solar wind are capable of producing a variety of temperature–density relationships. Since we strictly impose a polytropic relationship with γ = constant throughout our simulations, we conclude that a negative correlation between density and temperature cannot be used to infer the value of γ at a fixed location in space.

Our examples suggest that the negative correlation derives from variations in the thermodynamic entropy of the plasma. Our fifth example (Figures 2e and 8) shows that when the entropy of the perturbed gas remains the same as the ambient solar wind, the temperature–density relationship is a fair indicator of the polytropic index of the gas. In apparent contraction, however, in our third example (Figures 2c and 6), the pulse appears to maintain constant entropy (since it contains no variations in density or temperature), and yet does not yield a slope of 0.5. The concept of entropy we have been using, however, is strictly only applicable to individual parcels of plasma as they propagate away from the Sun and expand. A more realistic definition of entropy at a particular location in space, such as the inner boundary of our simulations, must take into account the speed of the plasma. Thus we suggest that entropy flux ($S \times v$) must be conserved for temperature–density relationships to be able to provide meaningful values of the polytropic index.

Our simulations support the idea suggested by *Gosling* [1999] that the negative correlation is the result of local pressure imbalances. However, other causes may be responsible. It is possible, for example, that the observed negative correlation derives from kinetic effects of the electrons, such as the idea proposed by *Hammond et al.* [1996], that are not included in the fluid simulations.

In addition to the results presented here, a number of interesting temperature–density relationships were found. One relatively common type consisted of a circular pattern in Log(T)–Log(n) space. Such a pattern suggests that within the ejecta, temperature and density go through phases of being positively correlated, uncorrelated, and negatively correlated. We are not aware of any corroborative observations of such variations. However, if such variations turn out to have observational counterparts, then plots of Log(T) versus Log(n) may provide a useful technique for identifying CME intervals within in situ data sets.

In closing, we reiterate that our simulations demonstrate that a negative correlation between density and temperature can exist for a variety of launch profiles, in spite of the fact that we strictly impose γ=constant in our model. Moreover, we suggest that the observed relationships are more indicative of entropy variations. In contrast to the conclusions reached by *Osherovich and Bulaga* [1997], we have shown that single–fluid hydrodynamic and MHD models can reproduce the types of observed temperature–density variations in magnetic clouds, sheath regions, and ambient solar wind, without resorting to non–physical arguments requiring γ<1.

Acknowledgements. PR gratefully acknowledges the support of the National Aeronautics and Space Administration (grant NASW–98007 and Space Physics Theory Program contract NAS5–96081). Work by JTG was performed under the auspices of the U.S. Department of Energy with support from NASA and the Ulysses project.

References

Fainberg, J., V. A. Osherovich, R. G. Stone, and R. J. MacDowall, Ulysses observations of electron and proton components in a magnetic cloud and related wave activity, in *Solar Wind Eight, Amer. Instit. Phys. Conf. Proceed. 382*, edited by D. Winterhalter, J. T. Gosling, S. R. Habbal, W. S. Kurth, and M. Neugebauer, New York, pp. 554–557, 1996.

Gosling, J. T., On the determination of electron polytrope indices within coronal mass ejections in the solar wind, submitted to *J. Geophys. Res.*, 1999.

Gosling, J. T., D. J. McComas, J. L. Phillips, L. A. Weiss, V. J. Pizzo, B. E. Goldstein, and R. J. Forsyth, A new class of forward–reverse shock pairs in the solar wind, *Geophys. Res. Lett., 21,* 2271, 1994.

Gosling, J. T., and P. Riley, The acceleration of slow coronal mass ejections in the high–speed solar wind, *Geophys. Res. Lett., 23,* 2867, 1996.

Gosling, J. T., P. Riley, D. J. McComas, and V. J. Pizzo, Overexpanding coronal mass ejections at high l\heliographic latitudes: Observations and simulations, *J. Geophys. Res., 103,* 1941, 1998.

Hammond, C. M., J. L. Phillips, G. K. Crawford, and A. Balogh, The relationship between electron density and temperature inside coronal mass ejections, in *Solar Wind Eight, Amer. Instit. Phys. Conf. Proceed. 382*, edited by D. Winterhalter, J. T. Gosling, S. R. Habbal, W. S. Kurth, and M. Neugebauer, New York, pp. 558–651, 1996.

Hundhausen, A. J., and R. A. Gentry, Numerical simulations of flare–generated disturbances in the solar wind, *J. Geophys. Res.*, 74, 2908, 1969.

Newbury, J. A., C. T. Russell, and G. M. Lindsay, Solar wind polytropic index in the vicinity of stream interactions, *Geophys. Res. Lett., 24,* 1431, 1997.

Osherovich, V. A., and L. F. Burlaga, Magnetic clouds, in Doronal Mass Ejections: Causes and consequences, Geophysical Monograph 99, edited by N. Crooker, J. A. Joselyn, and J. Feynman, Washington DC, pp 157–168, 1997.

Osherovich, V. A., C. J. Farrugia, L. F., Burlaga, R. L. Lepping, J. Fainberg, and R. G. Stone, Polytropic relationship in interplanetary magnetic clouds, *J. Geophys. Res., 98,* 15331, 1993a.

Osherovich, V. A., C. J. Farrugia, and L. F. Burlaga, Dynamics of aging magnetic clouds, *Adv. Space Res.*, 13(6), 57, 1993b.

Osherovich, V. A., C. J. Farrugia, and L. F. Burlaga, Nonlinear evolution of magnetic flux ropes 2. Finite beta plasma, *J. Geophys. Res., 100,* 12,307, 1995.

Osherovich, V. A., C. J. Farrugia, R. G. Stone, R. Fitzenreiter, and A. F. Vinas, Measurement of polytropic index in the January 10–11, 1997 magnetic cloud observed by WIND, *Geophys. Res. Lett., 25,* 3003, 1998.

Osherovich, V. A., C. J. Farrugia, and R. G. Stone, Multi–tube model for interplanetary magnetic clouds, *Geophys. Res. Lett., 26,* 401, 1999.

Phillips, J. L., S. J. Bame, J. T. Gosling, D. J. McComas, B. E. Goldstein, and A. Balogh, Solar wind thermal electrons from 1.15 to 5.34 AU: Ulysses observations, *Adv. Space Res., 13(6)* 47, 1993.

Phillips, J. L., W. C. Feldman, J. T. Gosling, and E. E. Scime, Solar wind plasma electron parameters based on aligned observations by ICE and Ulysses, *Adv. Space Res., 16(9)* 95, 1995.

Pilipp, W. G., H. Miggenrieder, K. –H. Muhlhauser, H. Rosenbauer, and R. Schwenn, Large–scale variations of thermal electron parameters in the solar wind between 0.3 and 1 AU, *J. Geophys. Res., 95,* 6305, 1990.

Pete Riley, CME dynamics in a structured solar wind, *Solar Wind 9,* edited by S. R. Habbal, R. Esser, J. V. Hollweg, and P. A. Isenberg, published by The American Institute of Physics, pp131–136, 1999.

Skoug, R. M., W. C. Feldman, J. T. Gosling, and D. J. McComas, Electron characteristics of coronal mass ejections observed in the solar wind by ACE/SWEPAM, Eos Transaction, American Geophysical Union, April 27, 1999.

Riley, P., and J. T. Gosling, Do coronal mass ejections implode in the solar wind?, *Geophys. Res. Lett., 25,* 1529, 1998.

Riley, P., J. T. Gosling, and V. J. Pizzo, A two–dimensional simulation of the radial and latitudinal evolution of a solar wind disturbance driven by a fast, high–pressure coronal mass ejection, *J. Geophys. Res., 102,* 14,677, 1997.

Sittler, E. C., and J. D. Scudder, An empirical polytrope law for solar wind thermal electrons between 0.45 and 4.76 AU: Voyager 2 and Mariner 10, *J. Geophys. Res., 85,* 5131, 1980.

Stone, J. M., and M. L. Norman, ZEUS–2D: A radiation magnetohydrodynamics code for astrophysical flows in two dimensions. I. The hydrodynamic algorithms and tests, *Astrophys. J., 80,* 753, 1992.

Figure Captions

Figure 1. Solar wind equilibrium solution. Speed (v), number density (n) and gas pressure (P) are plotted against heliocentric distance (R).

Figure 2. Four perturbations to the inner boundary of the equilibrium solution summarized in Figure 1. Speed (v), number density (n), and gas pressure (P) are plotted against time (t). (a) Combined bell–shaped density, temperature, and speed enhancement lasting 50 hours. (b) Bell–shaped density enhancement lasting 30 hours. (c) Box–shaped speed decrease lasting 30 hours. (d) Bell–shaped density decrease and corresponding temperature enhancement (to maintain constant pressure) lasting 10 hours. (e) Bell–shaped density enhancement and corresponding temperature enhancement (to maintain constant entropy) lasting 10 hours.

Figure 3. Simulated speed (v), number density (n), and gas pressure (P) versus heliocentric distance (R) at 55 and 194 hours following the launch of the pulse summarized in Figure 2a. The boundary of the pulse is marked by the two pairs of vertical lines in each panel.

Figure 4. Logarithmic plot of Temperature (T) versus number density (n) at R=2.5 AU for the pulse profile summarized in Figure 2a. A cross marks the ambient solar wind. Diamonds (dots) indicate the ejecta (sheath) region. The straight line is a least–squares fit to the ejecta interval.

Figure 5. Same parameters displayed as in Figure 4 for the pulse profile summarized in Figure 2b. The top panel shows results at 1.5 AU and the bottom panel shows results at 3.5 AU.

Figure 6. Same parameters displayed as in Figure 4 for the pulse profile summarized in Figure 2c. The top panel shows results at 1.5 AU and the bottom panel shows results at 3.5 AU.

Figure 7. Same parameters displayed as in Figure 4 for the pulse profile summarized in Figure 2d at R=3.5 AU.

Figure 8. Same parameters displayed as in Figure 4 for the pulse profile summarized in Figure 2e at R=3.5 AU.

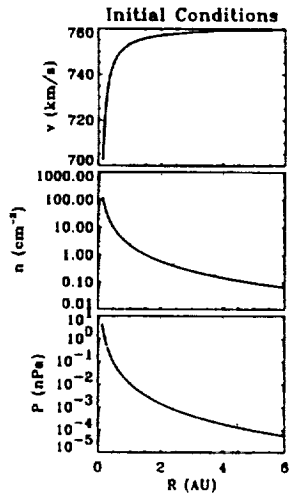
Initial Conditions
760
740
720
700
v (km/s)
1000.00
100.00
10.00
1.00
0.10
0.01
n (cm⁻³)
10¹
10⁰
10⁻¹
10⁻²
10⁻³
10⁻⁴
10⁻⁵
P (nPa)
0
2
4
6
R (AU)

Figure 1

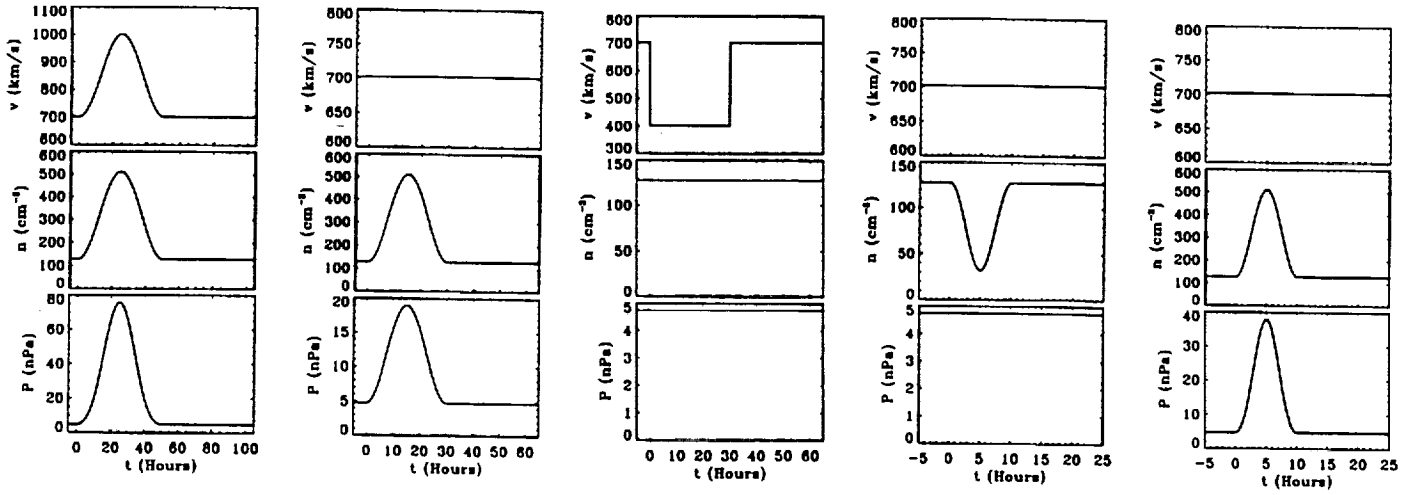

(a) (b) (c) (d) (e)

Figure 2

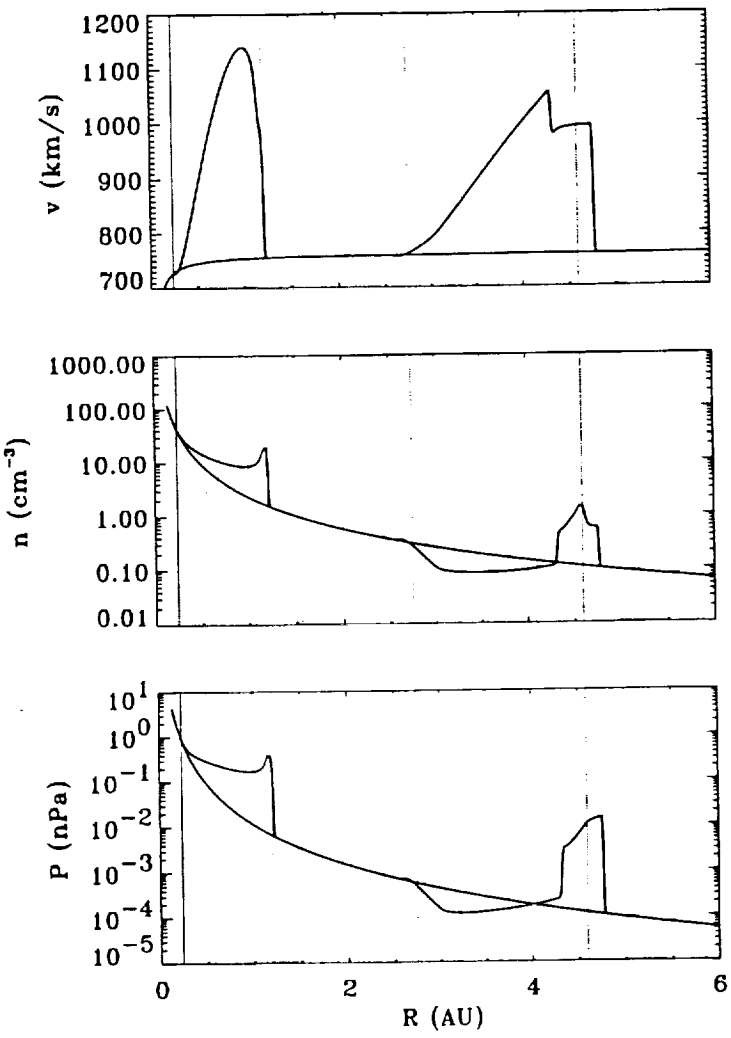
1200
1100
1000
900
800
700
v (km/s)
1000.00
100.00
10.00
1.00
0.10
0.01
n (cm^{-3})
10^{1}
10^{0}
10^{-1}
10^{-2}
10^{-3}
10^{-4}
10^{-5}
P (nPa)
0
2
4
6
R (AU)

Figure 3

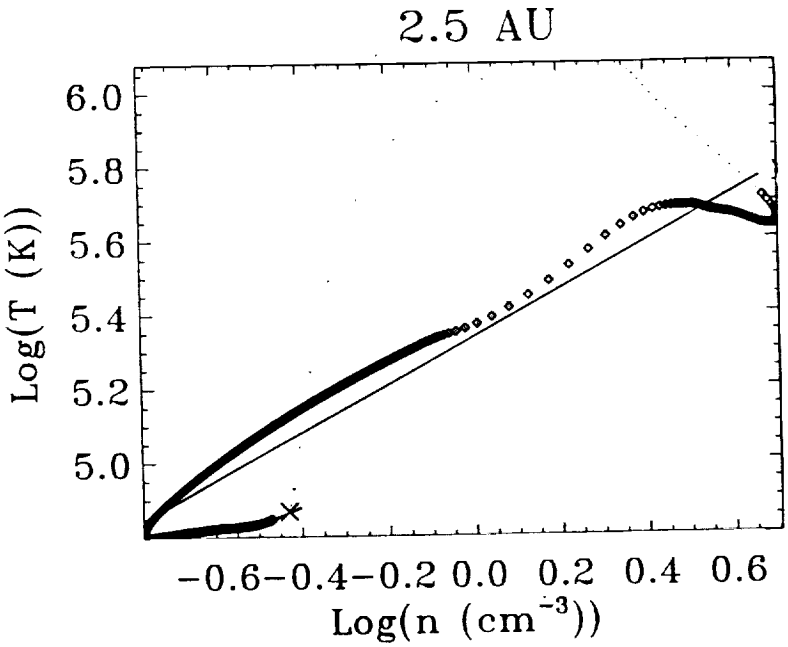

Figure 4

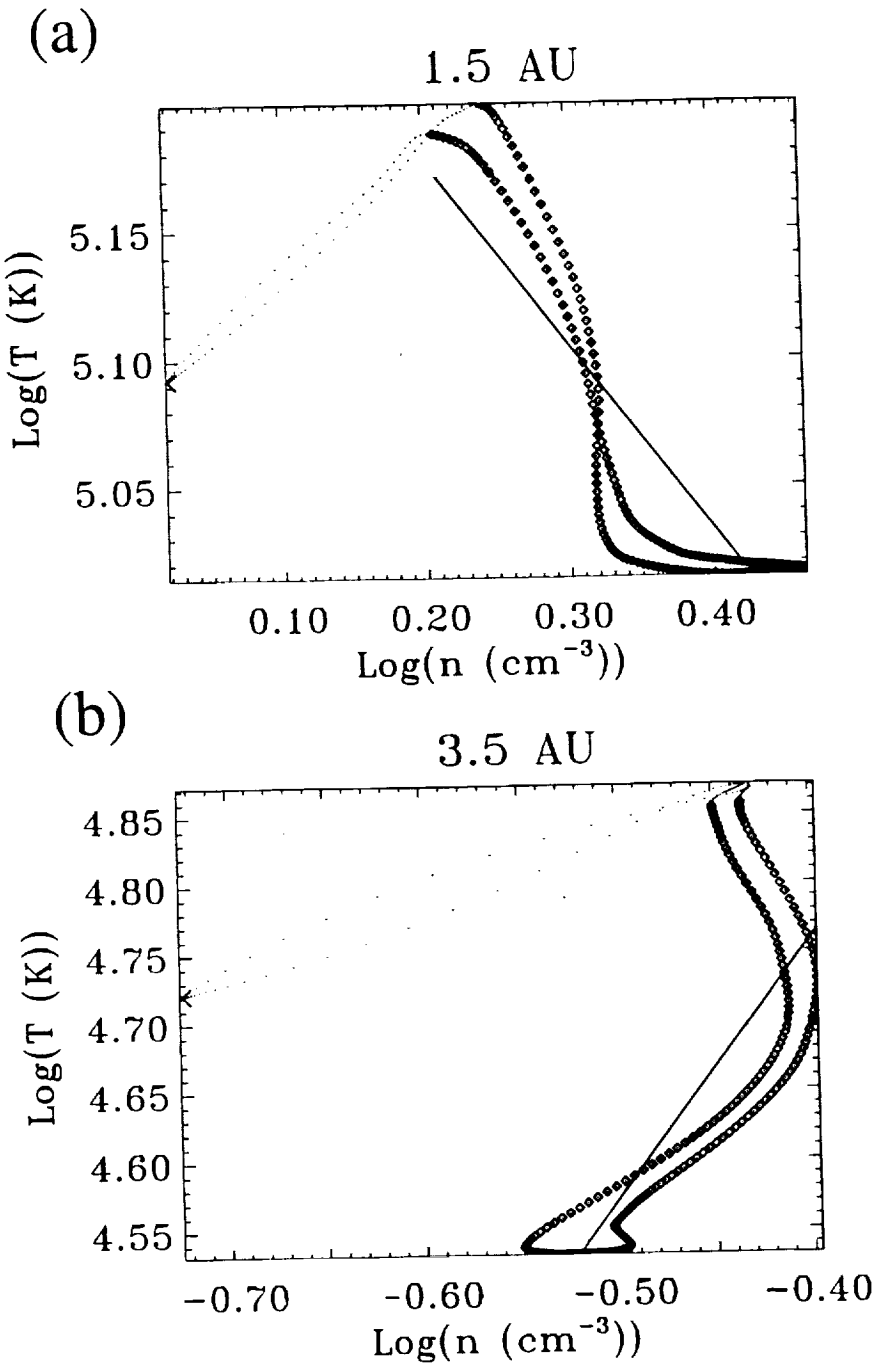
(a)
1.5 AU
5.15
5.10
5.05
Log(T (K))
0.10
0.20
0.30
0.40
Log(n (cm^{-3}))
(b)
3.5 AU
4.85
4.80
4.75
4.70
4.65
4.60
4.55
Log(T (K))
−0.70
−0.60
−0.50
−0.40
Log(n (cm^{-3}))

Figure 5

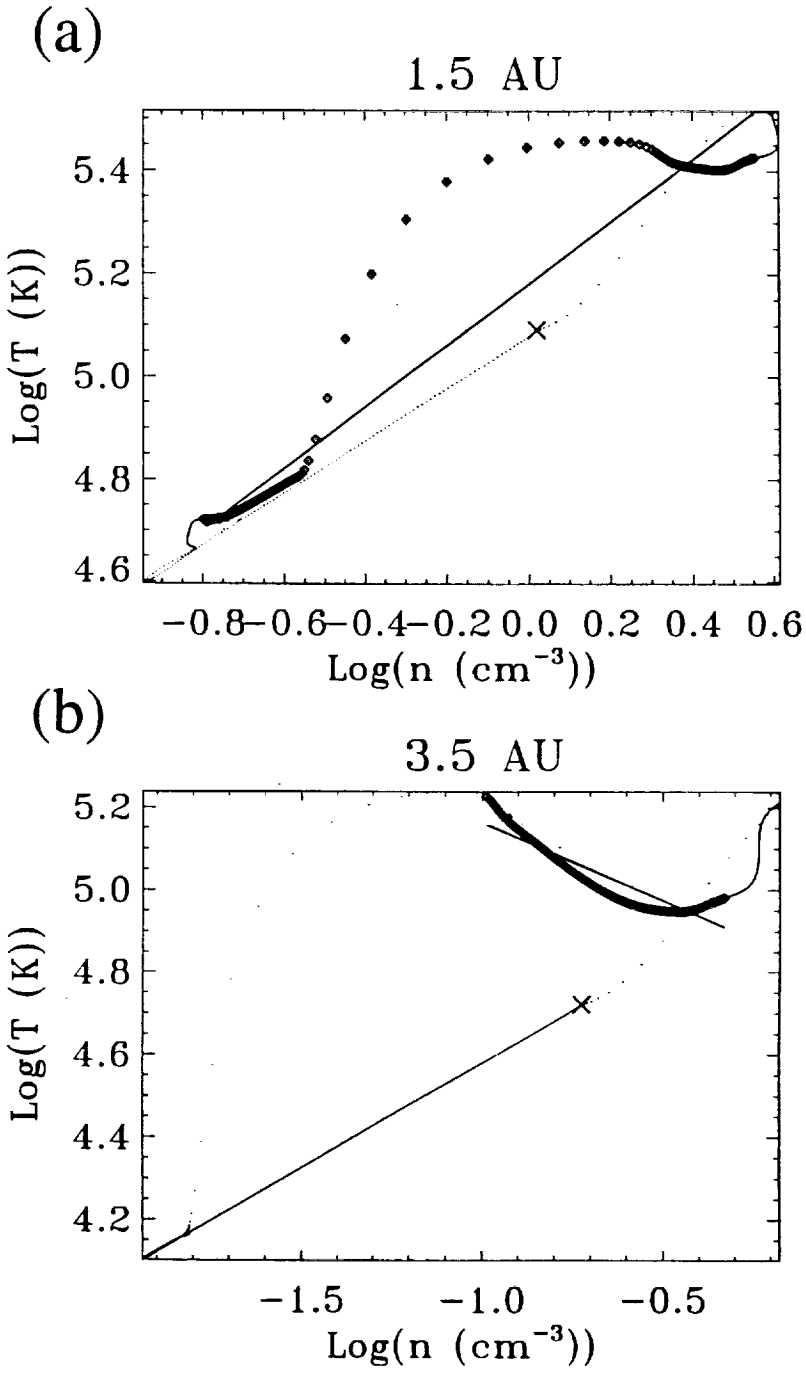
(a)
1.5 AU
5.4
5.2
5.0
4.8
4.6
Log(T (K))
−0.8 −0.6 −0.4 −0.2 0.0 0.2 0.4 0.6
Log(n (cm^{-3}))
(b)
3.5 AU
5.2
5.0
4.8
4.6
4.4
4.2
Log(T (K))
−1.5 −1.0 −0.5
Log(n (cm^{-3}))

Figure 6

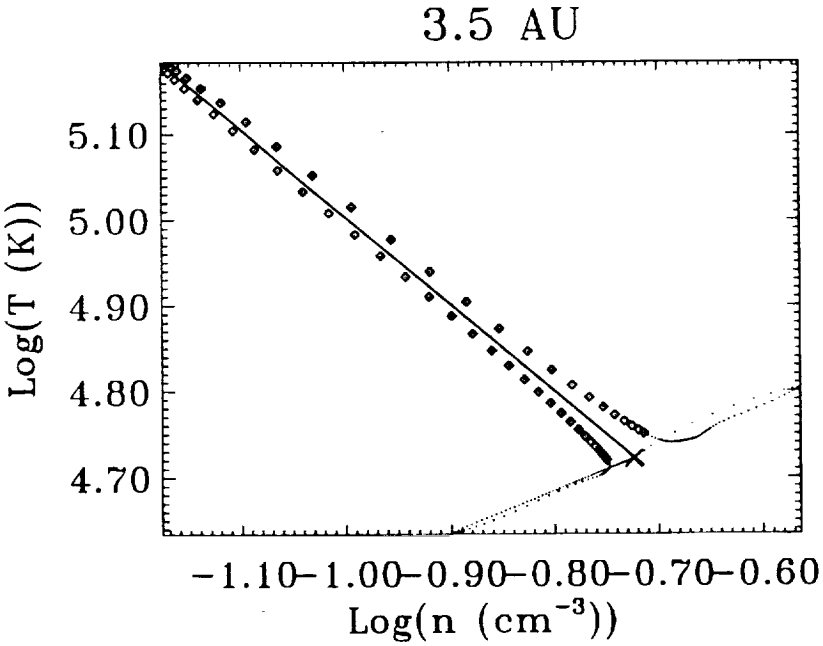

Figure 7

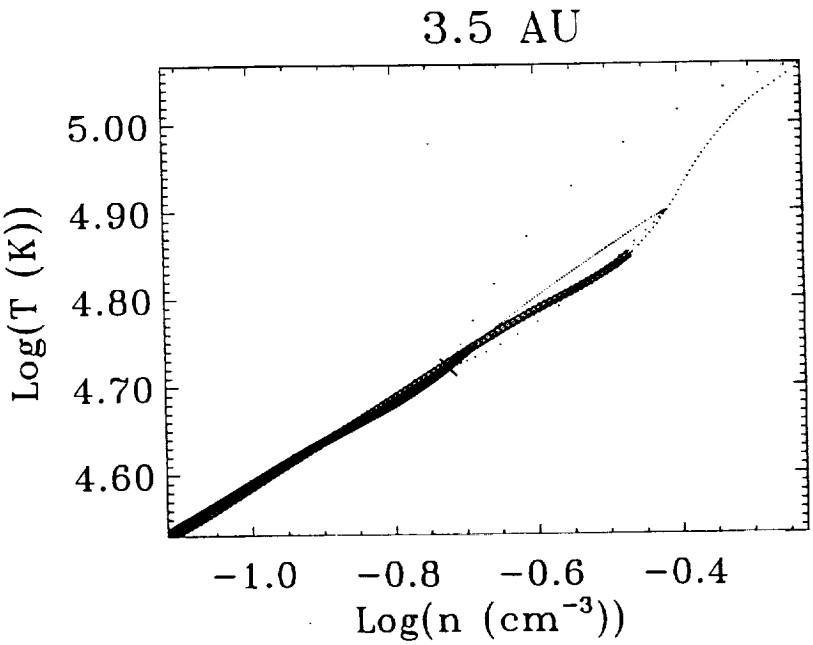

Figure 8

REPORT DOCUMENTATION PAGE

Form Approved
OMB No. 0704-0188

1. AGENCY USE ONLY *(Leave Blank)*	2. REPORT DATE	3. REPORT TYPE AND DATES COVERED
	02/23/00	Interim Contractor Report, 02/01/00- 02/29/00

4. TITLE AND SUBTITLE
An Investigation of the Large Scale Evolution and Topology of Coronal Mass Ejections in the Solar Wind

5. FUNDING NUMBERS
C: NASW-98007

6. AUTHOR(S)
Dr. Peter Riley

7. PERFORMING ORGANIZATION NAME(S) AND ADDRESS(ES)
SciberNet, Inc.
5414 Oberlin Drive, Suite 251
San Diego, CA 92121

8. PERFORMING ORGANIZATION REPORT NUMBER

9. SPONSORING / MONITORING AGENCY NAME(S) AND ADDRESS(ES)
National Aeronautics and Space Administration
Goddard Space Flight Center
Greenbelt, MD 20771

10. SPONSORING / MONITORING AGENCY REPORT NUMBER

11. SUPPLEMENTARY NOTES

12a. DISTRIBUTION / AVAILABILITY STATEMENT
Unclassified-Unlimited

12b. DISTRIBUTION CODE

13. ABSTRACT

This investigation (subcontract Sci-0201-99 of contract NASW-98007) is concerned with the large-scale evolution and topology of coronal mass ejections (CMEs) in the solar wind. During this reporting period (03/01/99 - 02/29/00) we have focused on several aspects of CME properties, their identification and their evolution in the solar wind. The work included both analysis of Ulysses and ACE observations as well as fluid and magnetohydrodynamic simulations. In addition, we analyzed a series of "density holes" observed in the solar wind, that bear many similarities with CMEs. Finally, this work was communicated to the scientific community at three meetings and has led to three scientific papers that are in various stages of review.

14. SUBJECT TERMS
Electron, Thermalization, Solar Wind, Planetary Plasma Boundaries

15. NUMBER OF PAGES
1

16. PRICE CODE

17. SECURITY CLASSIFICATION OF REPORT	18. SECURITY CLASSIFICATION OF THIS PAGE	19. SECURITY CLASSIFICATION OF ABSTRACT	20. LIMITATION OF ABSTRACT
Unclassified	Unclassified	Unclassified	UL